Mechanism of a COVID-19 nanoparticle vaccine candidate that elicits a broadly neutralizing antibody response to SARS-CoV-2 variants

Yi-Nan Zhang[1], Jennifer Paynter[1], Cindy Sou[1], Tatiana Fourfouris[1], Ying Wang[3,4], Ciril Abraham[3], Timothy Ngo[1], Yi Zhang[3,4], Linling He[1], and Jiang Zhu[1, 2, *]

[1]Department of Integrative Structural and Computational Biology, [2]Department of Immunology and Microbiology, The Scripps Research Institute, La Jolla, California 92037, USA

[3]Fels Institute for Cancer Research and Molecular Biology, and [4]Department of Microbiology and Immunology, Temple University, Philadelphia, Pennsylvania 19140, USA.

*Corresponding author

JZ: Phone +1 (858) 784-8157; Email: jiang@scripps.edu

KEYWORDS

Adjuvant; coronavirus disease 2019 (COVID-19); severe acute respiratory syndrome coronavirus 2 (SARS-CoV-2); variant of concern (VOC); vaccine; lymph node; germinal center; broadly neutralizing antibody (bNAb).

ABSTRACT (150 words)

Vaccines that induce potent neutralizing antibody (NAb) responses against emerging variants of severe acute respiratory syndrome coronavirus 2 (SARS-CoV-2) are essential for combating the coronavirus disease 2019 (COVID-19) pandemic. We demonstrated that mouse plasma induced by self-assembling protein nanoparticles (SApNPs) that present rationally designed S2GΔHR2 spikes can neutralize the B.1.1.7, B.1.351, and P.1 variants with titers comparable to the wildtype strain. The adjuvant effect on vaccine-induced immunity was illustrated by testing 16 formulations for the multilayered I3-01v9 SApNP that presents 20 stabilized spikes. Using single-cell sorting, monoclonal antibodies (mAbs) with diverse neutralization breadth and potency were isolated from mice immunized with the receptor binding domain (RBD), S2GΔHR2 spike, and SApNP vaccines. The mechanism of vaccine-induced immunity was examined in mice. Compared with the soluble spike, the I3-01v9 SApNP showed 6-fold longer retention, 4-fold greater presentation on follicular dendritic cell dendrites, and 5-fold stronger germinal center reactions in lymph node follicles.

ONE-SENTENCE SUMMARY (125 characters)

With prolonged lymph node retention and robust germinal centers, spike nanoparticles offer a vaccine solution to emerging SARS-CoV-2 variants.

INTRODUCTION

The COVID-19 pandemic has led to more than 152 million infection cases and 3.2 million deaths globally. Human antibody responses to SARS-CoV-2 spike antigens in COVID-19 patients can be sustained for several months after infection (*1-5*). However, recently identified variants of concern (VOCs) exhibit higher transmissibility and resistance to prior immunity as SARS-CoV-2 continues to adapt to the human host (*6, 7*). One such variant, B.1.1.7, emerged from southeast England in October 2020 and accounted for two-thirds of new infections in London in December 2020, with a higher transmission rate (43-90%) and risk of mortality (32-104%) than previously circulating strains (*8-11*). Other variants, such as B.1.351 and P.1, also became prevalent in three provinces in South Africa and in Manaus, Brazil, respectively (*7, 12-14*). A new variant, B.1.617, is now causing a second wave of COVID-19 in India (*15*). The rise of SARS-CoV-2 VOCs and their rapid spread worldwide will likely result in more infection cases, hospitalizations, and potentially more deaths, further straining healthcare resources (*14*).

To date, eight COVID-19 vaccines have been approved for emergency use in humans, with more than 90 candidates assessed in various phases of clinical trials (*16*). With the exception of inactivated whole-virion vaccines, diverse platforms have been used to deliver the recombinant SARS-CoV-2 spike, such as mRNA-encapsulating liposomes (e.g., BNT162b2 and mRNA-1273), adenovirus vectors (e.g., ChAdOx1 nCoV-19 [AZD1222], CTII-nCoV, Sputnik V, and Ad26.COV2.S), and micelle-attached spikes (e.g., NVX-CoV2373). These vaccines demonstrated 65-96% efficacy in Phase 3 trials, with lower morbidity and mortality associated with COVID-19 disease (*17-21*). However, a notable loss of vaccine efficacy against new SARS-CoV-2 variants was reported because of spike mutations in the receptor-binding domain (RBD; e.g., K417N, E484K, and N501Y), N-terminal domain (NTD; e.g., L18F, D80A, D215G, and Δ242-244), and

other regions that are critical to spike stability (e.g., D614G) (*7*, *22*-*29*). Among circulating VOCs, the B.1.351 lineage appeared to be most resistant to neutralization by convalescent plasma (9.4-fold) and vaccine sera (10.3 to 12.4-fold) (*30*), whereas a lesser degree of reduction was observed for an early variant, B.1.1.7 (*31*, *32*). Based on these findings, it was suggested that vaccines would need to be updated periodically to maintain protection against rapidly evolving SARS-CoV-2 (*25*, *33*, *34*). This raises the concern that herd immunity may not be achievable with current vaccines and highlights the necessity of developing vaccines that can elicit a broadly neutralizing antibody (bNAb) response to SARS-CoV-2 variants (*25*, *29*). As previously reported (*35*-*43*), the production of a bNAb response relies on long-lived germinal center (GC) reactions to activate precursor B cells, stimulate affinity maturation, and form long-term immune memory. Antigen retention and presentation within lymph node follicles are key to the induction of long-lived GC reactions (*35*, *37*, *44*, *45*) and should be considered in the development of bNAb-producing vaccines (*46*).

We previously investigated the cause of SARS-CoV-2 spike metastability and rationally designed the S2GΔHR2 spike, which was displayed on three self-assembling protein nanoparticle (SApNP) platforms, including ferritin (FR) 24-mer and multilayered E2p and I3-01v9 60-mers, as COVID-19 vaccine candidates (*47*). In the present study, we investigated the vaccine-induced NAb response to SARS-CoV-2 VOCs and mechanism by which SApNP vaccines (e.g., I3-01v9) generate such a response. We first examined the neutralizing activity of mouse plasma from our previous study (*47*) against three representative SARS-CoV-2 variants, B.1.1.7, B.1.351, and P.1. Mouse plasma induced by the spike-presenting I3-01v9 SApNP potently neutralized all three variants with comparable titers to the wildtype strain, Wuhan-Hu-1. When a different injection route was tested in mouse immunization, E2p and I3-01v9 SApNPs sustained neutralizing titers against the three VOCs, even at a low dosage of 3.3 μg, whereas a significant reduction of plasma

neutralization was observed for the soluble spike. Next, we examined the adjuvant effect on vaccine-induced humoral and T-cell responses for the I3-01v9 SApNP. While the non-adjuvanted group yielded detectable neutralizing titers, conventional adjuvants, such as aluminum hydroxide (AH) and phosphate (AP), boosted the titers by 8.6 to 11.3-fold (or 9.6 to 12.3 times). Adjuvants that target the stimulator of interferon genes (STING) and Toll-like receptor 9 (TLR) pathways enhanced neutralization by 21 to 35-fold, either alone or combined with AP, in addition to a Th1-biased cellular response. We then performed single-cell sorting to isolate 20 monoclonal antibodies (mAbs) from RBD, spike, and I3-01v9 SApNP-immunized mice. These mAbs were from diverse B cell lineages, of which some neutralized the wildtype SARS-CoV-2 strain and three VOCs with equivalent potency. Lastly, we investigated how SApNPs behave in lymph nodes and induce GCs by characterizing vaccine delivery and immunological responses at the intraorgan, intracellular, and intercellular levels in the mouse model. The spike-presenting I3-01v9 SApNP showed 6-fold longer retention, 4-fold greater presentation on follicular dendritic cell dendrites, and 5-fold higher GC reactions. Intact protein nanoparticles in lymph node tissues were visualized by transmission electron microscopy (TEM). Our study demonstrates that a spike-presenting SApNP vaccine may confer broad protection against diverse SARS-CoV-2 variants.

RESULTS

Spike and SApNP vaccine-induced neutralizing responses to SARS-CoV-2 variants.

We previously demonstrated that the rationally designed S2GΔHR2 spike was more immunogenic than the S2P spike (*48*), and SApNPs that present 8-20 spikes outperform soluble spikes in NAb elicitation (*47*) **(Fig. 1A)**. Notably, the I3-01v9 SApNP that presents 20 S2GΔHR2 spikes induced a potent NAb response to both SARS-CoV-1 and SARS-CoV-2, as well as critically needed T-cell responses (*47*). SARS-CoV-1 shares only modest sequence similarity (~73% in the RBD) with

SARS-CoV-2. Thus, we hypothesized that our vaccines would protect against emerging variants that are much more closely related to the wildtype SARS-CoV-2 strain, Wuhan-Hu-1.

We first assessed the neutralizing activity of polyclonal plasma induced by various spike and SApNP vaccine formulations from our previous study (*47*) against the wildtype SARS-CoV-2 strain, Wuhan-Hu-1, as a baseline for comparison (**Fig. 1B**). Mouse plasma collected at week 5 after two intraperitoneal (i.p.) injections of adjuvanted vaccine antigens (50 μg) was analyzed in pseudoparticle (pp) neutralization assays (*49*). The soluble $S2P_{ECTO}$ spike elicited the lowest 50% inhibitory dilution (ID_{50}) titers, whereas the soluble S2GΔHR2 spike increased neutralization with a 7.1-fold higher average ID_{50} titer, which did not reach statistical significance because of within-group variation. All three spike-presenting SApNPs elicited superior neutralizing responses to the soluble $S2P_{ECTO}$ spike (*47*). Notably, the I3-01v9 SApNP showed the most potent neutralizing response, with an average ID_{50} titer of 2090, which was 8.1-fold higher than the soluble $S2P_{ECTO}$ spike. Despite differences in ID_{50} titers, the overall pattern remained the same as reported in our previous study (*47*). The differences might be attributable to the inherent variation of pseudovirus neutralization assays (*49, 50*). We then assessed neutralizing activity against three major SARS-CoV-2 variants (**Fig. 1C**, **fig. S1A, B**). The I3-01v9 SApNP induced a stronger neutralizing response against three VOCs, with 0.5-fold (B.1.1.7), 0.8-fold (B.1.351), and 1.8-fold (P.1) higher (or 1.5-2.8 times) ID_{50} titers compared with the wildtype strain (**Fig. 1C**). Altogether, these results confirmed our hypothesis and highlighted the advantages of spike-presenting SApNPs.

Next, we examined the influence of injection dosage and route on the plasma neutralizing response to various SARS-CoV-2 strains. To this end, we performed a mouse study, in which three groups of mice were immunized with 5, 15, and 45 μg of I3-01v9 SApNP three times through i.p. injection. Remarkably, all three SARS-CoV-2 VOCs were neutralized by mouse plasma, with

comparable ID_{50} titers observed across dose groups (**fig. S1C, D**). To examine whether routes of injection affect the plasma neutralizing response against variants, we performed another mouse study, in which a low dose (3.3 μg) of adjuvanted antigen was intradermally administered into four footpads (i.e., 0.8 μg/footpad). The large (~55-60 nm) E2p and I3-01v9 SApNPs that present 20 S2GΔHR2 spikes yielded higher ID_{50} titers against the wildtype strain than the soluble S2GΔHR2 spike (**Fig. 1D**, **fig. S1E, F**), whereas a notable reduction of ID_{50} titers against the variants was noted for mouse plasma from the S2GΔHR2 group (**Fig. 1E**, **fig. S1E, F**), suggesting that multivalent display is critical for eliciting a broad neutralizing response. The E2p and I3-01v9 SApNP groups exhibited comparable or stronger plasma neutralization against three VOCs relative to the wildtype Wuhan-Hu-1 strain (**Fig. 1E**). In our previous study, a panel of human NAbs was used to evaluate the antigenicity of stabilized S2GΔHR2 spike and SApNPs and to validate the SARS-CoV-2-pp assays (*47*). In the present study, this panel of human NAbs was tested against SARS-CoV-2-pps that carry spikes of the wildtype strain and the three VOCs (**Fig. 1F**, **fig. S1G**). Lower potency against the B.1.351 and P.1 variants, measured by the 50% inhibitory concentration (IC_{50}), was observed for all human NAbs, with the exception of NAb S309, which was identified from a SARS-CoV-1 patient (*51*). This finding is consistent with reports on convalescent patient plasma (*30-32*). As a negative control, mouse plasma induced by the S2GΔHR2-presenting I3-01v9 SApNP was tested against pseudoviruses carrying the murine leukemia virus (MLV) envelope glycoprotein (Env), or MLV-pps. Nonspecific neutralization was not detected for samples produced in two independent immunization experiments (**fig. S1H, I**). Altogether, these results demonstrate that spike-presenting SApNPs are more advantageous than soluble spikes in eliciting a strong neutralizing response against SARS-CoV-2 variants.

Adjuvant effect on vaccine-induced neutralizing antibody and T-cell responses.

Innate immunity plays an important role in regulating the adaptive immunity, including humoral and cellular immune responses (*52-56*). Adjuvant-formulated vaccines have been shown to recruit and activate innate immune cells more effectively at injection sites and local lymph nodes (*57-60*). Among commonly used adjuvants, AH and AP create depots for the recruitment and activation of antigen-presenting cells (APCs) at injection sites and sentinel lymph nodes (*61, 62*), whereas oil-in-water emulsions (e.g., MF59) promote antigen retention and APC stimulation in lymph nodes (*63, 64*). Pattern recognition receptor agonists (e.g., STING, TLR3, TLR4, TLR7/8, and TLR9 agonists) stimulate APCs at injection sites and nearby lymph nodes (*52, 59, 65-72*). Macrophage inhibitors (e.g., clodronate liposomes, termed CL) directly stimulate B cells or inhibit antigen sequestration by subcapsular sinus macrophages, thus resulting in more effective GC simulation in lymph nodes (*73-75*). Adjuvant combinations may generate a synergistic immune response by simultaneously activating multiple pathways (*59, 68*).

To examine the effect of innate signaling pathways on SApNP-induced immune responses, we tested 16 adjuvant formulations in a systematic study (**Fig. 2A**), in which mice were immunized with the adjuvanted I3-01v9 SApNP (20 μg) via intradermal injections in four footpads (i.e., 5 μg/footpad). We first tested mouse plasma neutralization against the wildtype SARS-CoV-2 stain. Mouse plasma at week 5 was analyzed in SARS-CoV-2-pp assays (**Fig. 2B, fig. S2A, B)**. The non-adjuvanted group showed detectable neutralization after two doses, with an average ID_{50} titer of 160, which was used as a baseline in this analysis. By comparison, conventional adjuvants, such as AH, AP, and MF59 (AddaVax), increased ID_{50} titers by 10.3, 7.6, and 12.5-fold, respectively. The macrophage inhibitor CL boosted plasma neutralization by merely 1.6-fold relative to the non-adjuvanted group. Adjuvants that target pattern recognition receptors exhibited differential effects on plasma neutralization, increasing ID_{50} titers by 1.1 to 34.2-fold. Notably, STING and CpG

(TLR9) substantially enhanced neutralizing titers, whereas TLR3, TLR4, and TLR7/8 agonists only exerted a modest effect. In most cases, adjuvants combined with AP further boosted plasma neutralizing activity. For example, when TLR4 and TLR7/8 agonists were mixed with AP, a 3.1-fold increase in ID_{50} titers was observed, suggesting a synergistic effect of stimulating multiple immune pathways. Overall, STING and CpG, either alone or combined with AP, elicited a plasma neutralizing response superior to any other adjuvant or adjuvant mix, increasing ID_{50} titers by 21 to 34-fold compared with the non-adjuvanted group. This is consistent with the results of the S-Trimer (SCB-2019), which, when formulated with CpG 1018 (TLR9 agonist) and alum adjuvants, induced potent NAb responses in nonhuman primates and human trials (*76, 77*). Mouse plasma at week 8 showed further increases in ID_{50} titers (1 to 3-fold) for most adjuvant groups (**Fig. 2C, fig. S2C, D)**. Lastly, we examined mouse plasma at week 5 from the STING and CpG groups against the B.1.1.7, B.1.351, and P.1 variants (**Fig. 2C, fig. S2E, F)**. Both groups exhibited impressive neutralizing responses to the three VOCs, with ID_{50} titers comparable to the wildtype strain.

We previously demonstrated that the AP-formulated I3-01v9 SApNP induces interferon-γ (IFN-γ)-producing $CD4^+$ Th1 cells and IFN-γ/interleukin-4 (IL-4) double-positive memory $CD4^+$ T cells (*47*). Given the superior performance of STING and CpG in plasma neutralization, we examined the impact of these two adjuvants on vaccine-induced T-cell responses. IFN-γ-producing $CD4^+$ T helper (Th) cells are important for optimal antibody responses and the induction of cellular immunity to clear viruses (*78-80*). To assess the effect of STING and CpG on vaccine-induced Th cells, we isolated splenocytes from mice 8 weeks after vaccination and cultured them in the presence of BALB/c mouse dendritic cells (DCs) pulsed with the spike-presenting I3-01v9 SApNP. Compared with the non-adjuvanted control (PBS in the place of an adjuvant), STING and CpG (TLR9) induced 3.7 and 5.5-fold more IFN-γ-producing $CD4^+$ Th1 cells, and 5.5 and 16-fold

198 more IL-4-producing $CD4^+$ Th2 cells, respectively (**Fig. 2E**). A non-significant trend toward a
199 higher frequency of both Th1 and Th2 cells was observed in mice immunized with the CpG-
200 formulated I3-01v9 SApNP. Nonetheless, both adjuvants induced more IFN-γ-producing $CD4^+$
201 Th1 cells than IL-4-producing $CD4^+$ Th2 cells, suggesting a dominant Th1 response in these mice.
202 This is consistent with the results for the S-Trimer (SCB-2019), which, when formulated with the
203 AS03 adjuvant or mixed CpG 1018/alum adjuvants, induced Th1-biased cellular responses in mice
204 (*76*). STING and CpG also enhanced $CD8^+$ T-cell responses, by 6 and 10-fold, respectively,
205 compared with the PBS control. Notably, this effect was more visible for CpG in terms of both the
206 frequency and number of IFN-γ-producing $CD8^+$ effector T cells (**Fig. 2F**).

207 Our results demonstrate that the I3-01v9 SApNP itself is immunogenic and adjuvants can
208 further enhance vaccine-induced NAb responses in plasma by up to 35-fold. The I3-01v9 SApNP,
209 when formulated with the STING or TLR9 agonist, yielded the highest ID_{50} titers with robust
210 $CD4^+$ and $CD8^+$ T-cell responses, highlighting their potential as adjuvants in the development of
211 more effective SARS-CoV-2 vaccines.

212 **Diverse variant-neutralizing mouse antibody lineages identified by single-cell analysis.**
213 Although plasma neutralization confirmed the effectiveness of our newly designed SARS-CoV-2
214 vaccines (*47*) against VOCs, the nature of this response was unclear. It might result from multiple
215 NAb lineages that each target a specific strain (non-overlapping), a few bNAb lineages that are
216 each able to block multiple strains (overlapping), or a combination of both. Previously, we used
217 antigen-specific single-cell sorting to identify potent mouse NAbs elicited by an I3-01 SApNP that
218 presents 20 stabilized HIV-1 Env trimers (*81*). Here, we applied a similar strategy to decipher NAb
219 responses induced by SARS-CoV-2 vaccines using mouse samples from our previous study (*47*),
220 for which potent plasma neutralization against VOCs has been verified (**Fig. 1C**).

Spleen samples from M4 in the spike group (S2GΔHR2-5GS-1TD0) and M2 in the spike-SApNP group (S2GΔHR2-10GS-I3-01v9-L7P), along with a control sample from M2 in the RBD (RBD-5GS-1TD0) group were analyzed. Two probes, RBD-5GS-foldon-Avi and S2GΔHR2-5GS-foldon-Avi, were produced, biotinylated, and purified to facilitate antigen-specific B cell sorting (**fig. S3A**, **B**). Following antibody cloning, reconstituted mouse mAbs were tested for neutralizing activity against the wildtype strain, Wuhan-Hu-1, in SARS-CoV-2-pp assays. A total of 20 mAbs, four from the RBD group (**fig. S3C**), six from the spike group (**fig. S3D**), and 10 from the I3-01v9 SApNP group (**fig. S3E**), were found to be NAbs. The genetic analysis of mAb sequences revealed some salient features of the vaccine-induced NAb response in mice (**Fig. 3A**). Overall, these mAbs evolved from diverse germline origins. The RBD-elicited mAbs appeared to use distinct germline variable (V) genes for both heavy chain (HC) and κ-light chain (KC), or V_H and V_K, respectively, whereas the spike and I3-01v9 SApNP-elicited mAbs shared some common V_H genes, such as IGHV14-1/3 and IGHV1S81. This result was not unexpected because the RBD vaccine presents a structurally distinct antigen to the immune system compared with the spike and I3-01v9 vaccines, which both present the S2GΔHR2 spike. These mAbs showed low levels of somatic hypermutation (SHM) with respect to their germline genes. Heavy chain complementarity-determining region (HCDR3) loops ranged from 4 to 12 aa in length, whereas most KCs contained 9 aa KCDR3 loops. Collectively, diverse germline genes and HCDR3 loops, accompanied by low degrees of SHM, suggest that many antibody lineages must have been generated upon vaccination and some could achieve neutralizing activity without an extensive maturation process.

We then examined the biological function of these mouse mAbs. Neutralizing activity was assessed in SARS-CoV-2-pp assays against the wildtype strain and three VOCs (**Fig. 3B** and **fig. S3F**). Overall, diverse yet consistent patterns were observed for the three sets of mAbs. Both the

RBD vaccine (an RBD scaffold) and the two spike vaccines, albeit in different forms, appeared to elicit potent NAbs against the wildtype strain. MAbs TRBD-R-4G5, S2GD-S-2C10, and I3V9-R-1G9 showed similar IC_{50} values (0.019-0.030 μg/ml) against Wuhan-Hu-1, on par with the human NAbs CB6 (*82*) and CC12.1/3 (*83*) (**Fig. 1F**). All three vaccines elicited bNAb responses, despite variation in potency for different mAbs against different strains. Notably, I3V9-R-1G9, which was isolated from an SApNP-immunized mouse, demonstrated high potency across four SARS-CoV-2 strains (IC_{50}: 0.007-0.024 μg/ml). This bNAb provided evidence that individual bNAb lineages may critically contribute to the plasma neutralization of SARS-CoV-2 VOCs (**Fig. 1C**). All three vaccines generated NAbs that preferentially neutralize specific SARS-CoV-2 strains. Some mAbs, such as TRBD-R-4B6, S2GD-S-1F3, and I3V9-R-2E11, were more effective against the wildtype strain and an early VOC, B.1.1.7, whereas a subset of mAbs (e.g., TRDB-R-4F3 and S2GD-S-2E4) neutralized B.1.351 and P.1 with greater potency. Although RBD-isolated NAbs likely neutralized SARS-CoV-2 by blocking receptor binding, those spike-isolated NAbs may target the RBD, N-terminal domain (NTD), or epitopes in the S2 subunit. Thus, we tested these mAbs in an enzyme-linked immunosorbent assay (ELISA) against the RBD monomer and S2GΔHR2-5GS-1TD0 spike, both derived from the Wuhan-Hu-1 backbone (**Fig. 3C, fig. S3G, H**). Overall, all of the NAbs bound the RBD and spike with a half-maximal concentration (EC_{50}) of 0.034 μg/ml or lower, except for I3V9-R-2F2 (1.973 μg/ml for the RBD and 2.051 μg/ml for the spike). Most (15) NAbs showed greater binding affinity (or lower EC_{50} values) for the spike, suggesting that the two arms of the immunoglobulin (Ig) can each interact with one RBD of the spike, resulting in an avidity effect. Notably, more diverse binding patterns were observed for I3-01v9 SApNP-elicited NAbs. Although I3V9-S-1C9 and I3V9-S-1F5 bound to the spike more favorably than the RBD, indicated by 4.7 to 4.9-fold reduction in their EC_{50} values, three NAbs from this group (I3V9-R-

1G3 I3V9-R-1G9, and I3V9-R-2F10) preferred the monomeric RBD over the spike, which might be explained by steric hindrance when they approach the RBDs on a native-like spike.

Lastly, we characterized these mouse NAbs in antigen-specific B-cell repertoires by next-generation sequencing (NGS), as previously demonstrated for NAbs isolated from HIV-1 SApNP-immunized mice and rabbits (*81*). Using the same RBD and spike probes (**fig. S3A**), ~1500 splenic B cells were bulk-sorted from each of the three mice that were analyzed by single-cell sorting for mAb isolation (**fig. S4A**). Unbiased mouse antibody HC and KC libraries were constructed and sequenced on an Ion S5 platform, which yielded up to 4 million raw reads (**fig. S4B**). The antibody NGS data were then processed using a mouse antibodyomics pipeline (*84*) to remove low-quality reads, resulting in 0.11-0.41 full-length HCs and KCs (**Fig. S4B**). Quantitative profiles of critical antibody properties, such as germline gene usage, the degree of SHM, and CDR3 loop length, were determined for the RBD and spike-specific B cell populations (**fig. S4C**). All 20 single-cell-sorted mouse NAbs could well fall in the range of these repertoire profiles, but some V_H/V_K genes that accounted for large portions of antigen-specific B cells, such as IGHV9 and IGHV5, were not used by any NAbs, suggesting that they might give rise to non-neutralizing binding antibodies. Two-dimensional (2D) divergence/identity plots were generated to visualize these NAbs in the context of NGS-derived B-cell repertoires (**Fig. 3D**, **fig. S4D, E, F**). Somatic variants were identified for each NAb by searching for sequences of the same V_H/V_K gene with a CDR3 identity cutoff of 90% (or 85% for evolutionarily more remote variants). For the most potent NAb, TRBD-R-4G5, from an RBD-immunized mouse (M2), 34 HC variants were identified that overlapped with an "island" of high sequence similarity to TRBD-R-4G5 on the plot, whereas more KC variants (1183) were found, likely due to the lack of diversity in the KCDR3 region. A similar pattern was observed for the potent bNAb, I3V9-R-1G9, from an SApNP-immunized mouse (M2). By

comparison, fewer putative somatic variants were identified for other NAbs in the antigen-specific B cell repertoires irrespective the sorting probe used (**fig. S4D-F**), suggesting that these NAbs either were from less prevalent lineages or were generated in response to a previous injection (each mouse received four doses) (*47*). Similar observations were reported for the vaccination of non-human primates and humans in longitudinal repertoire analyses of single-cell-sorted NAbs (*85, 86*).

Single-cell isolation identified a panel of mouse mAbs with different neutralization breadth and potency against the wildtype SARS-CoV-2 strain and three major VOCs. The ELISA analysis suggested that the I3-01v9 SApNP can elicit NAbs with more diverse angles of approach to their epitopes than the RBD and soluble spike vaccine. Structural analysis by crystallography and EM may be needed to provide a more detailed understanding of NAb-antigen interactions.

Distribution and trafficking of I3-01v9 SApNP in mouse lymph node.

After validating these vaccines against VOCs at both the plasma and mAb levels, we studied *in vivo* behaviors of the S2GΔHR2 spike and two large SApNPs to understand why SApNPs outperform soluble spikes in bNAb elicitation. In principle, these SApNPs need to be transported to lymph nodes, retained, and presented to various immune cell populations to induce robust innate and adaptive immune responses. Here, we first examined the transport and distribution of I3-01v9 SApNPs in mouse lymph nodes via footpad injections (10 μg/footpad). The mice were sacrificed 12 h after single-dose (**Fig. 4A**) and prime-boost (**Fig. 4B**) regimens. The axillary, brachial, and popliteal sentinel lymph nodes were isolated for histological analysis. The lymph node tissues were stained with the human anti-spike antibody P2B-2F6 (*87*) to characterize SARS-CoV-2 spikes presented on the I3-01v9 SApNPs. Consistent with our previous study (*88*), SApNPs accumulated in lymph node follicles, regardless of the number of doses. SApNPs were sequestrated in the center

of lymph node follicles after a single dose (**Fig. 4A,** images on the left, schematics on the right) but were located along the outer layer of expanded lymph node follicles after the second injection due to preexisting humoral immunity (i.e., GC reactions) that was induced by the first dose (**Fig. 4B**, images on the left, schematics on the right). Overall, the majority of SApNPs accumulated in lymph node follicles, but their distribution differed slightly depending on the doses.

In this context, we examined patterns of trafficking and lymph node follicle retention for soluble S2GΔHR2 spike *vs*. the S2GΔHR2-presenting E2p and I3-01v9 SApNPs. To facilitate this analysis, the mice were sacrificed 2 h to 8 weeks after a single dose (**Fig. 4C**) and 2 h to 5 weeks after the boost (**Fig. 4D**). The injection dose was normalized to the total amount of protein (10 μg) per injection into each footpad (40 μg/mouse). As shown in **Fig. 4C**, the S2GΔHR2 spikes that trafficked into lymph node follicles at 2 h cleared within 48 h. In contrast, the two large SApNPs accumulated in the subcapsular sinus at 2 h and then trafficked into follicles 12 h after the single-dose injection. Remarkably, I3-01v9 SApNPs remained detectable in lymph node follicles after 2 weeks, suggesting 6-fold longer retention than the S2GΔHR2 spike (**Fig. 4C**). The results for these protein nanoparticles are thus consistent with the pattern of size dependency that was observed for ovalbumin-conjugated gold nanoparticles in our previous study (*88*), in which small (5-15 nm) nanoparticles cleared shortly after the injection, whereas large (50-100 nm) nanoparticles were retained in lymph node follicles for weeks. Similar patterns of antigen retention were observed after the second injection, although the boost appeared to exert a more positive effect on the soluble spike, which could be detected in lymph node follicles at 48 h (**Fig. 4D**). Nonetheless, prolonged retention was observed for both E2p and I3-01v9 SApNPs 2 weeks after the boost injection. Overall, the multivalent display of S2GΔHR2 spikes on the I3-01v9 SApNP resulted in 325- and 4-fold greater accumulation in lymph node follicles compared with the soluble spike 48 h after the

single-dose **(Fig. 4E**) and prime-boost (**Fig. 4F**) injections, respectively. These findings reveal the advantage of a leading vaccine candidate identified in our previous study, S2GΔHR2-10GS-I3-01v9-L7P (*47*), in terms of spike antigen retention in lymph node follicles.

Retention and presentation of I3-01v9 SApNP on follicular dendritic cell dendrites.

Antigen retention and presentation in lymph node follicles are prerequisites to the stimulation of robust B cell responses and GC reactions (*35, 37, 89*). Resident cells spatially rearrange antigens and present them to B cells. Follicular dendritic cells (FDCs) are resident stromal cells in follicles and retain soluble antigens, immune complexes, virus-like particles, viruses, and bacteria (*88, 90-94*). FDCs are also key to GC initiation, maintenance, and B-cell affinity maturation (*40, 95-98*). Here, we hypothesized that FDCs comprise the major cell population in lymph node follicles that retain SARS-CoV-2 spikes and spike-presenting SApNPs. To test this hypothesis, we administered vaccines via footpad injections and collected mouse lymph nodes at the peak of accumulation (12 h) after single-dose (**Fig. 5A**) and prime-boost (**Fig. 5B**) injections. Lymph node tissue samples were stained with the anti-spike antibody P2B-2F6 (*87*) for the S2GΔHR2 spike, as well as anti-CD21 and anti-CD169 antibodies for FDCs and subcapsular sinus macrophages, respectively. The spike and SApNP (E2p or I3-01v9) signals colocalized with FDC ($CD21^+$) networks in lymph node follicles (**Fig. 5A, B**). This result confirmed the critical role of FDC networks in mediating vaccine retention in lymph node follicles.

The induction of potent bNAb responses by spike-presenting SApNPs in mice suggests the effective activation of naïve B cells and subsequent recalls by crosslinking B cell receptors (*94, 99-102*). We visualized the interface between FDC networks and B cells to better understand how FDC networks present SApNPs to engage B cells. Briefly, fresh lymph nodes were isolated and directly immersed in fixative. The processed tissue samples were sectioned and stained on copper

grids for TEM analysis. We first determined whether SApNPs, such as the S2GΔHR2-presenting I3-01v9 SApNP, remain intact *in vivo* (**fig. S5**). Mouse lymph nodes were isolated 2 h after the injection of a high dose (50 μg) of the non-adjuvanted I3-01v9 SApNP. The TEM images revealed that round-shape granules corresponding to intact SApNP aligned on the macrophage surface or inside endolysosomes of the macrophage in a lymph node (**fig. S5**). We next studied the relative location between FDCs and I3-01v9 SApNPs and how FDCs present SApNPs to B cells. Mouse lymph nodes were collected 2, 12, and 48 h after a single-dose (50 μg) and 12 h after the boost of the I3-01v9 SApNP vaccine. The FDCs exhibited the characteristic morphology of long dendrites that surrounded and interacted with B cells in lymph node follicles (**Fig. 5C**, **fig. S6**). Few I3-01v9 SApNPs were observed on FDC dendrites at 2 h (**fig. S6D**), whereas notably more nanoparticles migrated to and aligned on FDC dendrites at 12 and 48 h (**Fig. 5C**, **fig. S6A-C**, yellow arrows). The TEM images indicated that FDCs can present many SApNPs to neighboring B cells in this "hugging mode", in which their long dendrites brace B cells to maximize interactions between multivalently displayed spikes and B cell receptors. These results demonstrated the intrinsic nature of FDCs as a reservoir for the sequestration, retention, and presentation of virus-like particles, or SApNPs with similar molecular traits, to initiate GC reactions.

Robust germinal center reactions induced by spike-presenting SApNPs.

Long-lived GC reactions induce immune stimulation for B-cell selection and affinity maturation and the production of immune memory and bNAb responses (*35, 36, 46*). Here, we investigated whether the prolonged retention of S2GΔHR2-presenting E2p and I3-01v9 SApNPs induce more robust GCs in lymph node follicles than the soluble S2GΔHR2 spike. Immunohistological analysis was performed to characterize GC B cells ($GL7^+$) and T follicular helper (T_{fh}) cells ($CD4^+Bcl6^+$). For the I3-01v9 SApNP, 2 weeks after immunization, we observed robust GCs in lymph node B

cell follicles ($B220^+$) with well-formed dark zone (DZ) and light zone (LZ) compartments, which contain GC B cells, FDCs, and T_{fh} cells (*36*, *38*, *103-107*) (**Fig. 6A**). We then extended the analysis to the S2GΔHR2 spike and spike-presenting SApNPs 2, 5, and 8 weeks after the single-dose injection (**Fig. 6B, fig. S7A-C**) and 2 and 5 weeks after the boost (**Fig. 6C, fig. S7D, E**). Two metrics, the GC/FDC ratio (i.e., whether GC formation is associated with an FDC network, %) and GC size (i.e., occupied area), were used. Overall, the soluble spike and both large SApNPs induced robust GCs 2 weeks after immunization (**Fig. 6B, fig. S7A**). The E2p and I3-01v9 SApNPs that present 20 spikes induced robust, long-lived GCs, whereas the spike alone failed to sustain robust GCs at week 8 with either the single-dose (**Fig. 6B, D**) or prime-boost (**Fig. 6C, E**) injections. The I3-01v9 SApNP generated larger GCs than the soluble spike, 2.0-fold larger after the single dose (**Fig. 6B, D**) and 2.4-fold larger after the boost (**Fig. 6C, E**), measured at week 8.

We further characterized GC reactions by flow cytometry. Fresh mouse lymph nodes were disaggregated into a single cell suspension and stained with an antibody cocktail to quantify GC B cells and T_{fh} cells (**fig. S8A**). The results were consistent with the immunohistological analysis, in which all spike-based vaccine antigens, including the S2GΔHR2 spike and SApNPs, showed robust GCs at week 2 after the injection that declined over time, as measured at weeks 5 and 8 (**Fig. 6F**). The E2p and I3-01v9 SApNPs generated a larger population of GC B cells than both the $S2P_{ECTO}$ and S2GΔHR2 spikes at week 2 (**fig. S8B, C**). Although the boost dose had little impact on the frequency of GC B cells and T_{fh} cells, it appeared to extend GC formation within lymph nodes (**Fig. 6F, G**), which may promote B cell development toward bNAbs. Notably, the GC B cell and T_{fh} cell populations elicited by the soluble S2GΔHR2 spike were barely detectable 5 weeks after immunization (**Fig. 6F, G**). This result was reminiscent of a recent study of an mRNA vaccine, in which GC reactions diminished to baseline levels at week 4 after a single-dose

injection (*108*). The S2GΔHR2-presenting I3-01v9 SApNP generated 3.7/5.2-fold more GC B cells and 3.7/4.4-fold more T_{fh} cells than the soluble S2GΔHR2 spike at week 8 after one/two-dose immunization (**Fig. 6F, G**). Therefore, SApNPs that were retained on FDC dendrites could present NAb epitopes to enable more effective B cell recognition than the soluble spike, and consequently induce more robust and long-lived GCs in lymph nodes. Patterns of trafficking and retention may be specific to antigen size, as shown previously (*88*) and in the present study (**Figs. 4** and **5**), but GC reactions are largely determined by vaccine adjuvants. This effect was briefly demonstrated for the E2p and I3-01v9 SApNPs, which were previously formulated with the AddaVax and AP adjuvants (*47*). At week 2 after a single-dose injection, the adjuvanted SApNPs induced stronger GC reactions than the non-adjuvanted groups (**fig. S9**). This result can also explain the differences in plasma neutralization between the adjuvanted and non-adjuvanted I3-01v9 SApNPs **(Fig. 2)**.

NGS has been used to assess vaccine-draining lymph node B cell responses (*109*). Here, we characterized lymph node B cells at the repertoire level for three groups of mice immunized with two doses (3.3 μg each) of the S2GΔHR2 spike, E2p, and I301v9 SApNPs via footpad injections. At this dosage, the spike showed less effective plasma neutralization against VOCs than the large SApNPs (**Fig. 1E**). Given their differences in retention, presentation, and GC reaction (**Figs. 4-6**), they were expected to yield different lymph node B-cell profiles. Interestingly, antigen-specific sorting identified more spike-targeting lymph node B cells from the I3-01v9 SApNP group than both the spike and E2p SApNP groups (**fig. S10A**). The antibody NGS data were processed by the mouse antibodyomics pipeline (*84*) (**fig. S10B**) to derive repertoire profiles for all three groups (**fig. S10C-E**). Compared with the spike, the I3-01v9 SApNP appeared to activate fewer V_H/V_K genes (**fig. S10F**, left two), while generating a larger population of spike-specific lymph

node B cells (**fig. S10A**). This pattern was different from the analysis of GC B cells at week 5 after two injections, albeit at a higher (40 μg) dosage (**Fig. 6G**). Importantly, the spike and SApNP groups showed a similar degree of SHM for V_H genes (**fig. S10F**, middle left), in contrast to more mutated V_H genes observed for hepatitis C virus (HCV) E2 core SApNPs (*110*). Notably, I3-01v9 showed higher SHM for V_K genes than E2p (**fig. S10F**, middle right). The I3-01v9 SApNP induced lymph node B cells exhibited highly consistent HCDR3 loop length across animals with little variation, as measured by the root-mean-square fluctuation (RMSF) (**fig. S10F**, right two). The unexpected lymph node B-cell profiles thus revealed the complex inner workings of a primary site for vaccine-induced immunity. The I3-01v9 SANP exhibited more "focused" B-cell activation and development in vaccine-draining lymph nodes. More studies are needed to determine the factors (e.g., SApNP carrier and adjuvant) that contribute to this selectivity.

DISCUSSION

To end the COVID-19 pandemic, vaccines need to effectively block current and emerging SARS-Cov-2 variants that evade NAb responses by mutating key epitopes on the viral spike (*25*). To overcome this challenge, some suggested that COVID-19 vaccines need to be updated on a regular basis (*25, 33, 34*), whereas others developed mosaic or cocktail vaccines based on currently known variants (*111, 112*). These vaccine strategies may not provide long-term solutions as SARS-CoV-2 is evolving rapidly and will acquire new mutations to evade vaccine-induced immunity (e.g., B.1.617) (*15*). In our previous study (*47*), the spike-presenting SApNPs induced a potent NAb response to SARS-CoV-1, which is evolutionarily more distant to the wildtype SARS-CoV-2 strain, Wuhan-Hu-1, than all its circulating variants. Based on this finding, we hypothesized that the spike-presenting SApNPs may provide an effective vaccine solution against SARS-CoV-2

variants. In the present study, we sought to confirm this hypothesis by testing three major VOCs and, if proven true, investigate the mechanism underlying such a broadly protective vaccine.

We explored several critical aspects related to vaccine effectiveness, with a focus on the lead candidate identified in our previous study, S2GΔHR2-10GS-I3-01v9-L7P (*47*). We first tested vaccine-induced mouse plasma, which represents a polyclonal response, against three SARS-CoV-2 VOCs. Mouse plasma generated previously (*47*) and in new studies using different regimens (e.g., injection route, dosage, and adjuvant) potently neutralized the variants. Notably, SApNPs retained their high ID_{50} titers at a dosage as low as 3.3 μg, whereas formulation with the STING and TLR9 agonists further enhanced the I3-01v9 SApNP-induced neutralizing response. Plasma neutralization may be sensitive to assay variation (*50*) and should be interpreted with caution, but single-cell-sorted mAbs provided unambiguous evidence of the vaccine-induced bNAb response. Our results revealed that a plethora of NAb lineages were generated upon vaccination, with I3-01v9 SApNP being the most effective at eliciting bNAbs. Protein vaccines, despite the well-established records of safety and effectiveness, have yet to be deployed to mitigate the COVID-19 pandemic (*113-116*). One protein vaccine, NVX-CoV2373 (micelle-attached spikes formulated with the Matrix-M™ adjuvant), showed 96.4% efficacy in human trials (*117*). Our studies demonstrate that SApNPs that present 20 stabilized spikes may provide a superior protein vaccine candidate that can be used either alone or as a booster for current nucleic acid vaccines (e.g., mRNA and viral vectors) in the battle against emerging SARS-CoV-2 variants (*15*).

We explored the mechanism of SApNP vs. spike vaccines following the previously used strategy to analyze the *in vivo* behaviors of antigen-attached gold nanoparticles (*88*). In principle, SApNP vaccines must induce long-lasting GCs to facilitate the development of bNAbs. Effective vaccine retention and presentation are critical for inducing and sustaining GC reactions, which in

473 turn promote the proliferation and affinity maturation of antigen-specific B cells. Indeed, we found
474 that the I3-01v9 SApNP, our lead vaccine candidate (*47*), elicited 6-fold longer retention and 4-
475 fold greater accumulation in lymph node follicles than the stabilized S2GΔHR2 spike alone with
476 a prime-boost regimen. This can be attributed to the intrinsic physiological properties of lymph
477 nodes that mediate vaccine trafficking and retention in follicles in a size-dependent manner, which
478 would favor retaining large (> 50 nm) virus-like particles (*88, 90, 91, 102, 118, 119*). Supporting
479 this notion are the TEM images of retained SApNPs aligned on long FDC dendrites, suggesting
480 that such protein nanoparticles can present spike antigens to B cells for rapid initiation and then
481 sustain GC reactions in lymph node follicles for an extended period of time. Specifically, the I3-
482 01v9 SApNP generated 2.4-fold larger GCs and greater numbers of GC B cells (5.2-fold) and T_{fh}
483 cells (4.4-fold) than the soluble S2GΔHR2 spike with the prime-boost regimen. These findings
484 provide quantitative evidence that spike-presenting SApNPs are uniquely suited for inducing long-
485 lived robust GCs in lymph node follicles. Our analyses thus shed light on the mechanism by which
486 the I3-01v9 SApNP can elicit a more effective bNAb response than the soluble spike (*33*).

487 As postulated by Burton and Topol, an in-depth understanding of bNAbs will facilitate the
488 rational design of more effective SARS-CoV-2 vaccines (*25*). Superior NAb responses have been
489 reported for some vaccine candidates that take advantage of particulate display (*111, 120-131*).
490 The S2GΔHR2-presenting I3-01v9 SApNP elicited a potent bNAb response to three VOCs, thus
491 overcoming a major challenge. Mechanistic studies of trafficking, retention, presentation, and GC
492 reactions can provide much-needed insights into vaccine-induced immunity (*116, 132-134*). Such
493 knowledge, once obtained for different vaccine platforms, such as inactivated whole virions,
494 mRNAs, viral vectors, individual spikes, and SApNPs, will facilitate rational selection of the most
495 effective vaccine candidate for SARS-CoV-2 other other pathogens.

MATERIALS AND METHODS

SARS-CoV-2 spike and SApNP vaccine antigens

The design, expression, and purification of a stabilized SARS-CoV-2 spike, S2GΔHR2, and three SApNPs that present either 8 or 20 S2GΔHR2 spikes were described in our recent study (*47*). Briefly, the spike gene of the SARS-CoV-2 isolate Wuhan-Hu-1 (GenBank accession no. MN908947) was modified to include the mutations ^{682}GSAGSV^{687} and K986G/V987G, in addition to truncation of the HR2 stalk (ΔE1150-Q1208). The viral capsid protein SHP (Protein Data Bank: 1TD0) was added as a C-terminal trimerization motif to stabilize the S2GΔHR2 trimer, resulting in a soluble S2GΔHR2-5GS-1TD0 spike (*47*). The S2GΔHR2 spike was genetically fused to FR, multilayered E2p, and multilayered I3-01v9 with 5GS, 5GS, and 10GS linkers, respectively, resulting in three S2GΔHR2-presenting SApNPs (*47*). An S2P$_{ECTO}$-5GS-1TD0 spike construct that contained the mutations ^{682}GSAGSV^{687} and K986G/V987G but without HR2 deletion (*47*) was included for comparison. All vaccine antigens were transiently expressed in ExpiCHO cells and purified by a CR3022 antibody column and size-exclusion chromatography (SEC) as described previously (*47*). Briefly, ExpiCHO cells were thawed and incubated with ExpiCHO™ Expression Medium (Thermo Fisher) in a shaker incubator at 37 °C, 135 rotations per minute (rpm), and 8% CO_2. When the cells reached a density of 10×10^6 ml^{-1}, ExpiCHO™ Expression Medium was added to reduce cell density to 6×10^6 ml^{-1} for transfection. The ExpiFectamine™ CHO/plasmid DNA complexes were prepared for 100-ml transfection in ExpiCHO cells following the manufacturer's instructions. For a given construct, 100 μg of plasmid and 320 μl of ExpiFectamine™ CHO reagent were mixed in 7.7 ml of cold OptiPRO™ medium (Thermo Fisher). After the first feed on day one, ExpiCHO cells were cultured in a shaker incubator at 33 °C, 115 rpm and 8% CO_2 following the Max Titer protocol with an additional feed on day 5

(Thermo Fisher). Culture supernatants were harvested 13-14 days after transfection, clarified by centrifugation at 4000 rpm for 25 min, and filtered using a 0.45 μm filter (Thermo Fisher). The CR3022 antibody column was used to extract SARS-CoV-2 antigens from the supernatants, followed by SEC on a Superdex 200 10/300 GL column (for scaffolded RBD trimers), a Superose 6 16/600 GL column (for the S2GΔHR2 spike, with and without Avi-tag), or a Superose 6 10/300 GL column (for SApNPs). Protein concentration was determined using UV_{280} absorbance with theoretical extinction coefficients.

Animal immunization and sample collection

Similar immunization protocols were reported in our previous vaccine studies (*47*, *110*, *135*, *136*). Briefly, Institutional Animal Care and Use Committee (IACUC) guidelines were followed for all of the animal studies. BALB/c mice (6 weeks old) were purchased from The Jackson Laboratory and kept in ventilated cages in environmentally controlled rooms at The Scripps Research Institute. The mouse studies were conducted according to Association for the Assessment and Accreditation of Laboratory Animal Care guidelines, and the protocols were approved by the IACUC. For the immunogenicity study, the mice were intraperitoneally immunized at either week 0 or 3 with 200 μl of antigen/adjuvant mix containing 5-50 μg of vaccine antigen and 100 μl of adjuvant (*47*) or immunized at weeks 0 and 3 with 20 μl of antigen/adjuvant mix containing 0.8 μg of vaccine antigen per injection (3.3 μg/mouse) and 10 μl of adjuvant per injection (four footpads were injected with 80 μl, or 20 μl/footpad) via intradermal footpad injections. For the mechanistic study of vaccine trafficking, retention, and induced GCs, the mice were immunized at weeks 0 and 3 with 20 μl of antigen/adjuvant mix containing 10 μg of vaccine antigen and 10 μl of adjuvant per injection. To visualize the I3-01v9 SApNPs in lymph node tissues using TEM, the mice were immunized at weeks 0 and 3 with 70 μl of antigen/adjuvant mix containing 50 μg of vaccine

antigen and 20 µl of adjuvant per injection. Vaccines were administered into intradermal footpads of mice using a 29-gauge insulin needle under 3% isoflurane anesthesia with oxygen. Blood was drawn from the maxillary/facial vein into an ethylenediaminetetraacetic acid (EDTA)-coated tube 2 weeks after each immunization. Blood plasma was isolated after centrifugation at 14000 rpm for 10 min. Plasma was heated and inactivated at 56°C for 30 min. The supernatant was then collected after centrifugation at 8000 rpm for 10 min. Plasma was used to determine NAb responses in the pseudovirus neutralization assays. The axillary, brachial, and popliteal sentinel lymph nodes were collected at the end timepoint for further analysis.

Experimental adjuvants and formulation

The adjuvants squalene-oil-in-water (AddaVax), aluminum hydroxide (AH), aluminum phosphate (AP), 2'3'-c-di-AM(PS)2 (Rp,Rp) (STING ligand), monophosphoryl lipid A from S. minnesota (MPLA-SM) R595 (TLR4 agonist), imidazoquinoline compound R848 (TLR7/8 agonist), and CpG ODN 1826, Class B (murine) (TLR9 agonist) were purchased from InvivoGen. PIKA, a TLR3 agonist with enhanced T cell and antibody responses reported for a Phase I rabies vaccine trial (*137*), was used as an adjuvant. PIKA was generously provided by Yisheng Biopharma and included in this study as an adjuvant that activates the TLR3 pathway. Macrophage inhibitors clodronate liposomes (Liposoma BV CP-005-005) were used to eliminate subcapsular sinus macrophages in lymph nodes to promote more robust B cell activation. Mouse immunization was performed to examine the adjuvant effect for the I3-01v9 SApNP formulated with 16 adjuvants or adjuvant combinations and compare with non-adjuvanted I3-01v9 SApNP (PBS in the place of an adjuvant). Adjuvants were mixed with vaccine antigen 10 min before immunization. The mice were intradermally immunized at weeks 0, 3, 6 with 30-35 µl of antigen/adjuvant mix containing 5 µg of vaccine antigen I3-01v9 SApNP (20 µg per mouse) and 20-25 µl of adjuvant per injection

(four footpads were injected with a total of 120-140 μl). Mouse blood was isolated at week 5 and 8 after 2 and 3 intradermal injections, respectively. Spleens and lymph nodes were harvested at week 8 for immunological analyses. Spleen samples were ground through a 70 μm cell strainer to release splenocytes into a cell suspension. Splenocytes were spun down at 400 × *g* for 10 min, washed with PBS, and treated with ammonium-chloride-potassium (ACK) lysing buffer (Lonza). Solenocytes were then frozen with 3 ml of Bambanker freezing media.

SARS-CoV-2 pseudovirus neutralization assay

The SARS-CoV-2-pp neutralization assays were described in our previous study (*47*). Briefly, SARS-CoV-2-pps were generated by the co-transfection of HEK293T cells with the HIV-1 pNL4-3.lucR-E- plasmid (obtained from the National Institutes of Health AIDS reagent program; https://www.aidsreagent.org/) and the expression plasmid encoding the *S* gene of various SARS-CoV-2 strains, including three variants: B.1.1.7, B.1.351, and P.1 (GISAID accession no. EPI_ISL_601443, EPI_ISL_678597, and EPI_ISL_792680, respectively). The HEK293T-hACE2 cell line (catalog no. NR-52511) and pcDNA3.1(-) vector containing the *S* gene of the SARS-CoV-2 isolate Wuhan-Hu-1 (catalog no. NR52420) were requested from the BEI Resources (https://www.beiresources.org/) on September 23, 2020 and used in the pseudovirus neutralization assays (*49*). Based on sequence alignment, spike mutations were incorporated into the S gene of the original Wuhan-Hu-1 isolate (catalog no. NR52420) to create respective expression plasmids for B.1.1.7, B.1.351, and P.1. SARS-CoV-2-pp neutralization by immunized mouse plasma and human or mouse mAbs was performed according to our previously described protocol (*47*). Using the same co-transfection expression system as described above for the SARS-CoV-2-pps, we produced pseudoviruses carrying the murine leukemia virus (MLV) Env, MLV-pps, for use as a negative control (*47*). Percent neutralization data were analyzed using GraphPad Prism 9.0.2

software. ID_{50}/IC_{50} values were calculated using constraints for percent neutralization (0-100%), whereas unconstrained neutralization plots are shown in **Figs. 1** and **figs. S1-S3**.

Enzyme-linked immunosorbent assay

Each well of a Costar™ 96-well assay plate (Corning) was first coated with 50 µl PBS containing 0.2 µg of the appropriate antigens. The plates were incubated overnight at 4 °C, and then washed five times with wash buffer containing PBS and 0.05% (v/v) Tween 20. Each well was then coated with 150 µl of blocking buffer consisting of PBS and 40 mg/ml blotting-grade blocker (Bio-Rad). The plates were incubated with blocking buffer for 1 h at room temperature, and then washed five times with wash buffer. Mouse mAbs, in the immunoglobulin G (IgG) form, were diluted in the blocking buffer to a maximum concentration of 10 µg/ml followed by a 10-fold dilution series. For each dilution, a total volume of 50 µl was added to the appropriate wells. Each plate was incubated for 1 h at room temperature and then washed five times with PBS containing 0.05% Tween 20. A 1:5000 dilution of horseradish peroxidase (HRP)-conjugated goat anti-human IgG antibody (Jackson ImmunoResearch Laboratories) was then made in wash buffer (PBS containing 0.05% Tween 20), with 50 µl of this diluted secondary antibody added to each well. The plates were incubated with the secondary antibody for 1 h at room temperature, and then washed six times with PBS containing 0.05% Tween 20. Finally, the wells were developed with 50 µl of TMB (Life Sciences) for 3-5 min before stopping the reaction with 50 µl of 2 N sulfuric acid. The resulting plate readouts were measured at a wavelength of 450 nm. The ELISA data were analyzed to calculate EC_{50} values using GraphPad Prism 9.0.2 software.

Histology, immunostaining, and imaging

609 The mice were sacrificed 2 h to 8 weeks after a single-dose and 2 h to 5 weeks after the boost
610 immunization. The axillary, brachial, and popliteal sentinel lymph nodes were isolated for
611 histological analysis. Fresh lymph nodes were rapidly merged into frozen section compound
612 (VWR International, catalog no. 95057-838) in a plastic cryomold (Tissue-Tek at VWR, catalog
613 no. 4565) using liquid nitrogen to preserve the antigens on the cell membrane and spike. Lymph
614 node samples were stored at -80°C and sent to the Centre for Phenogenomics on dry ice for further
615 sample processing. Tissue sections (8 μm) were cut on a cryostat (Cryostar NX70) and collected
616 on charged slides. Sections were post-fixed in 10% neutral buffered formalin and permeabilized
617 in PBS containing 0.5% Triton X-100 before immunostaining. Protein Block (Agilent) was used
618 to block nonspecific antibody binding before incubating the sections with primary antibody
619 overnight at 4°C. After washing in TBST, the sections were incubated in fluorophore-conjugated
620 secondary antibodies for 1 h at room temperature. Lymph node tissue sections were stained with
621 human anti-spike antibody P2B-2F6 (*87*) (1:50) and biotinylated goat anti-human secondary
622 antibody (Abcam, catalog no. ab7152, 1:300), followed by streptavidin-HRP reagent (Vectastain
623 Elite ABC-HRP Kit, Vector, catalog no. PK-6100) then DAB (ImmPACT DAB, Vector, catalog
624 no. SK-4105) to study the distribution and retention of the S2GΔHR2 spike alone and S2GΔHR2-
625 presenting E2p and I3-01v9 SApNPs. For immunofluorescent staining, tissue sections were
626 stained for FDCs using anti-CD21 antibody (Abcam, catalog no. ab75985, 1:1800) followed by
627 anti-rabbit secondary antibody conjugated with Alexa Fluor 555 (Thermo Fisher, catalog no.
628 A21428; 1:200), stained for B cells using anti-B220 antibody (eBioscience, catalog no. 14-0452-
629 82, 1:100) followed by anti-rat secondary antibody conjugated with Alexa Fluor 674 (Thermo
630 Fisher, catalog no. A21247; 1:200), and stained for subcapsular sinus macrophages using anti-
631 sialoadhesin (CD169) antibody (Abcam, catalog no. ab53443, 1:600) followed by anti-rat

secondary antibody conjugated with Alexa Fluor 488 (Abcam, catalog no. ab150165; 1:200). Germinal center B cells were labeled using rat anti-GL7 antibody (FITC; BioLegend, catalog no. 144604, 1:250). T_{fh} cells were labeled using CD4 antibody (BioLegend, catalog no. 100402, 1:100) followed by anti-rat secondary antibody conjugated with Alexa Fluor 488 (Abcam, catalog no. ab150165; 1:1000) and Bcl6 antibody (Abcam, catalog no. ab220092, 1:300) followed by anti-rabbit secondary antibody conjugated with Alexa Fluor 555 (Thermo Fisher, catalog no. A21428; 1:1000). Nuclei were then counterstained with DAPI (Sigma-Aldrich, catalog no. D9542, 100 ng/ml). The stained tissue sections were scanned using an Olympus VS-120 slide scanner and imaged using a Hamamatsu ORCA-R2 C10600 digital camera for all bright-field and fluorescent images. Bright-field images of stained S2GΔHR2 spike and S2GΔHR2-presenting SApNPs in lymph node follicles and fluorescent images of GCs were quantified using ImageJ software (National Institutes of Health) (*138*).

Electron microscopy analysis of protein nanoparticles and lymph node tissues

Electron microscopy (EM) analysis was performed by the Core Microscopy Facility at The Scripps Research Institute. For the negative-staining EM analysis of protein nanoparticles, the S2GΔHR2-10GS-I3-01v9-L7P SApNP samples were prepared at the concentration of 0.01 mg/ml. Carbon-coated copper grids (400 mesh) were glow-discharged, and 10 µl of each sample was adsorbed for 2 min. Excess sample was wicked away, and grids were negatively stained with 2% uranyl formate for 2 min. Excess stain was wicked away and the grids were allowed to dry. For the EM analysis of mouse tissues, the lymph nodes were dissected from each animal and immersed in oxygenated 2.5% glutaraldehyde and 4% paraformaldehyde in 0.1M Na cacodylate buffer (pH 7.4) fixative overnight at 4ºC (*139*). After washing in 0.1 M sodium cacodylate buffer, the tissue samples were post-fixed in buffered 1% osmium tetroxide and 1.5% potassium ferrocyanide for 1-1.5 h at 4°C,

rinsed in the same buffer, and then stained *en bloc* with 0.5% uranyl acetate overnight at 4°C. The tissue samples were washed in double-distilled H_2O and dehydrated through a graded series of ethanol followed by acetone, infiltrated with LX-112 (Ladd) epoxy resin, and polymerized at 60°C. Ultrathin lymph node sections (at 70-nm thickness) were prepared for imaging. Samples were analyzed at 80 kV with a Talos L120C transmission electron microscope (Thermo Fisher), and images were acquired with a CETA 16M CMOS camera.

Lymph node disaggregation, cell staining, and flow cytometry

Germinal center reactions, including the percentage of GC B cells ($GL7^+B220^+$) and T_{fh} cells ($CD3^+CD4^+CXCR5^+PD1^+$), and the number of GC B cells and T_{fh} cells were studied by flow cytometry (**fig. S5A**). The mice were sacrificed 2, 5, and 8 weeks after a single-dose and 2 and 5 weeks after the boost immunization. Fresh axillary, brachial, and popliteal sentinel lymph nodes were collected and mechanically disaggregated. These lymph node samples were merged in enzyme digestion solution containing 958 μl of Hanks' balanced salt solution (HBSS) buffer (Thermo Fisher Scientific, catalog no. 14185052), 40 μl of 10 mg/ml collagenase IV (Sigma-Aldrich, catalog no. C5138), and 2 μl of 10 mg/ml of DNase (Roche, catalog no. 10104159001) in an Eppendorf tube. After incubation at 37°C for 30 min, lymph node samples were filtered through a 70 μm cell strainer and spun down at 400 × *g* for 10 min. The supernatant was discarded, and the cell pellet was resuspended in HBSS blocking solution containing 0.5% (w/v) bovine serum albumin and 2 mM EDTA. The nonspecific binding of Fc receptors was blocked using anti-CD16/32 antibody (BioLegend, catalog no. 101302) on ice for 30 min. Cocktail antibodies, Zombie NIR live/dead stain (BioLegend, catalog no. 423106), Brilliant Violet 510 anti-mouse/human CD45R/B220 antibody (BioLegend, catalog no. 103247), FITC anti-mouse CD3 antibody (BioLegend, catalog no. 100204), Alexa Fluor 700 anti-mouse CD4 antibody

(BioLegend, catalog no. 100536), PE anti-mouse/human GL7 antibody (BioLegend, catalog no. 144608), Brilliant Violet 605 anti-mouse CD95 (Fas) antibody (BioLegend, catalog no. 152612), Brilliant Violet 421 anti-mouse CD185 (CXCR5) antibody (BioLegend, catalog no. 145511), and PE/Cyanine7 anti-mouse CD279 (PD-1) antibody (BioLegend, catalog no. 135216) were then mixed with the cells and placed on ice for 30 min. After washing cells with HBSS blocking solution after antibody staining, the samples were fixed using 1.6% paraformaldehyde (Thermo Fisher Scientific, catalog no. 28906) in HBSS on ice for 30 min. The cell samples were stored in HBSS blocking solution for the flow cytometry study. Sample events were acquired by a 5-laser BD Biosciences LSR II analytical flow cytometer with BD FACS Diva 6 software at the Core Facility of The Scripps Research Institute. The data were further processed using FlowJo 10 software.

DC production, T cell culture, activation, and flow cytometry analysis

Mouse bone marrow (BM) was cultured in RPMI 1640 medium containing 10% fetal bovine serum and recombinant mouse Flt3L (50 ng/mL) and SCF (10 ng/ml) for 9 days as described (*140*). To induce DC activation, immature DCs were incubated with lipopolysaccharide (LPS, 100 ng/mL) plus R848 (Resiquimod, 100 ng/mL)) overnight, which activated TLR4 or TLR7/8 signaling, respectively. Cells were harvested for experiments. $CD11c^+$ DCs were sorted using magnetic beads (Miltenyi-Biotech, CA). Splenic mononuclear cells from each group of immunized mice were cultured in the presence of DCs pulsed with or without I3-01v9 SApNP (1×10^{-7} mM) in complete IMDM medium containing IL-2 (5.0 ng/ml). Cells were collected 16 h later for intracellular cytokine staining and flow cytometry. All antibodies used for immunofluorescence staining were purchased from eBioscience (San Diego, CA), BioLegend (San Diego, CA) or BD Biosciences (San Jose, CA). Magnetic microbead-conjugated streptavidin was purchased from Miltenyi-Biotech (Auburn, CA). Recombinant human IL-2 protein was purchased from R&D Systems

(Minneapolis, MN). Recombinant mouse Flt3 ligand (Flt3L) and mouse SCF were purchased from Shenandoah Biotech (Warwick, PA). Cells were stained with appropriate concentrations of mAbs. Dead cells were excluded using Fixable Viability Dye from eBioscience (San Diego, CA). Flow cytometry was performed using LSRII (BD Bioscience, CA).

Bulk and single-cell sorting of SARS-CoV-2 antigen-specific mouse B cells.

Spleens or lymph nodes were harvested from mice 15 days after the last immunization, and the cell suspension was prepared. Dead cells were excluded by staining with the Fixable Aqua Dead Cell Stain kit (Thermo Fisher L34957). FcγIII (CD16) and FcγII (CD32) receptors were blocked by adding 20 µl of 2.4G2 mAb (BD Pharmigen, catalog no. N553142). The cells were then incubated with 10 µg of a biotinylated RBD-5GS-foldon-Avi trimer or a biotinylated S2GΔHR2-5GS-foldon-Avi spike. Briefly, the probes were generated by the biotinylation of Avi-tagged SARS-CoV-2 antigens using biotin ligase BirA according to the manufacturer's instructions (Avidity). Biotin excess was removed by SEC on either a Superdex 200 10/300 column (GE Healthcare) for the RBD probe or a HiLoad Superose 6 16/600 column (GE Healthcare) for the spike probe. In the SEC profiles, the probe peak was well separated from the peak of biotin ligase (**fig. S3A**). Cells and biotinylated proteins were incubated for 5 min at 4 °C, followed by the addition of 2.5 µl of anti-mouse IgG fluorescently labeled with FITC (Jackson ImmunoResearch catalog no. 115-095-071) and incubated for 15 min at 4 °C. Finally, 5 µl of premium-grade allophycocyanin (APC)-labeled streptavidin was added to the cells and incubated for 15 min at 4 °C. In each step, the cells were washed with 0.5 ml of PBS and the sorting buffer, PBS with 2% FBS. $FITC^+$ APC^+ probe-specific B cells were sorted using MoFloAstrios EQ (Beckman Coulter). For bulk sorting, positive cells were sorted into an Eppendorf microtube with 20 µl of lysis buffer. For single B-cell sorting, individual positive cells were sorted into the inner wells of a 96-well

plate with 20 µl of pre-reverse transcription (RT) lysis mix containing 0.1 µl of NP40 (Sigma-Aldrich), 0.5 µl of RNAse Inhibitor (Thermo Fisher), 5 µl of 5× First Strand Buffer, and 1.25 µl of DTT from SuperScript IV kit (Invitrogen), with 13.15 µl of H_2O per well.

Antibody cloning from Env-specific single B cells and antibody production.

The antibody cloning of SARS-CoV2-2 antigen-sorted single B cells was conducted as follows. A mix containing 3 µl of Random Hexamers (GeneLink), 2 µl of dNTPs, and 1 µl of SuperScript IV enzyme (Thermo Fisher) was added to each well of a single-cell-sorted 96-well plate that underwent thermocycling according to the program outlined in the SuperScript IV protocol, resulting in 25 µl of cDNA for each single cell. cDNA (5 µl) was then added to a polymerase chain reaction (PCR) mix containing 12.5 µl of 2× Multiplex PCR mix (Qiagen), 9 µl of H_2O, 0.5 µl of forward primer mix, and 0.5 µl of reverse mouse primer mix (*141*) for heavy and κ-light chains within each well. A second PCR reaction was then performed using 5 µl of the first PCR as the template and respective mouse primers (*141*) according to the same recipe as the first PCR. The PCR products were run on 1% Agarose gel and those with correct heavy and light chain bands were then used for Gibson ligation (New England Biolabs), cloning into human IgG expression vectors, and transformation into competent cells. Mouse mAbs were expressed by the transient transfection of ExpiCHO cells (Thermo Fisher) with equal amounts of paired heavy and κ-light chain plasmids. Antibody proteins were purified from the culture supernatant after 12-14 days using Protein A bead columns (Thermo Fisher).

NGS and bioinformatics analysis of mouse B cells.

Previously, a 5′-rapid amplification of cDNA ends (RACE)-PCR protocol was reported for the unbiased sequencing of mouse B-cell repertoires (*84*). In the present study, this protocol was

applied to analyze bulk-sorted, RBD/spike-specific mouse B cells. Briefly, 5´-RACE cDNA was obtained from bulk-sorted B cells of each mouse with the SMART-Seq v4 Ultra Low Input RNA Kit for Sequencing (TaKaRa). The IgG PCRs were set up with Platinum *Taq* High-Fidelity DNA Polymerase (Life Technologies) in a total volume of 50 µl, with 5 µl of cDNA as the template, 1 µl of 5´-RACE primer, and 1 µl of 10 µM reverse primer. The 5′-RACE primer contained a PGM/S5 P1 adaptor, and the reverse primer contained a PGM/S5 A adaptor. We adapted the mouse 3´-C_γ1-3/3´-C_μ inner primers and 3´-mC_κ outer primer (*141*) as reverse primers for the 5´-RACE PCR processing of heavy and κ-light chains. A total of 25 cycles of PCR was performed and the expected PCR products (500-600 bp) were gel purified (Qiagen). NGS was performed on the Ion S5 GeneStudio system. Briefly, heavy and κ-light chain libraries from the same mouse were quantitated using a Qubit® 2.0 Fluorometer with Qubit® dsDNA HS Assay Kit and then mixed at a 3:1 ratio before being pooled with antibody libraries of other mice at an equal ratio for sequencing. Template preparation and (Ion 530) chip loading were performed on Ion Chef using the Ion 520/530 Ext Kit, followed by sequencing on the Ion S5 system with default settings. The mouse Antibodyomics pipeline (*84*). was used to process raw NGS data, derive quantitative profiles for germline gene usage, degree of SHM, and H/KCDR3 loop length, and generate 2D divergence/identity plots to visualize mAbs in their respective repertoires.

Statistical analysis

Data were collected from 4-7 mice per group. All of the statistical analyses were performed and graphs were generated using GraphPad Prism 6.01 software. For the antibody analysis, comparisons between different vaccine groups were performed using two-tailed unpaired Student's *t*-test. Comparisons of neutralizing antibody titers against SARS-CoV-2 variants were performed using the same plasma samples and analyzed using two-tailed paired Student's *t*-test.

769 For the vaccine accumulation and GC study as well as the adjuvant study, comparisons between
770 different vaccine groups were performed using one-way analysis of variance (ANOVA) followed
771 by Tukey's multiple comparison *post hoc* test. Statistical significance was determined as ns: not
772 significant, *$p < 0.05$, **$p < 0.01$, ***$p < 0.001$, ****$p < 0.0001$.
773

774 **SUPPLEMENTARY MATERIALS**

775 Supplementary material for this article is available at http://xxx/xxx/xxx.

776 **fig. S1**. Spike and spike-presenting SApNP vaccine-induced neutralizing antibody responses
777 against the wildtype SARS-CoV-2 strain and three variants of concern (VOCs).

778 **fig. S2.** Neutralizing antibody responses against the wildtype SARS-CoV-2 strain and three VOCs
779 induced by the S2GΔHR2-10GS-I3-01v9-L7P SApNP formulated with different adjutants.

780 **fig. S3.** Single-cell isolation and functional evaluation of monoclonal neutralizing antibodies from
781 mice immunized with the RBD, spike, and SApNP vaccines.

782 **fig. S4.** Unbiased repertoire analysis of bulk-sorted SARS-CoV-2 antigen-specific mouse splenic
783 B cells and tracing of mouse neutralizing antibodies in the NGS-derived repertoires.

784 **fig. S5**. SARS-CoV-2 spike-presenting SApNP interaction with macrophages in a lymph node.

785 **fig. S6**. TEM images of SARS-CoV-2 spike-presenting I3-01v9 SApNP interaction with FDCs in
786 a lymph node.

787 **fig. S7**. Immunohistological analysis of SARS-CoV-2 spike/spike-presenting SApNP vaccine-
788 induced GCs.

789 **fig. S8**. Flow cytometry analysis of SARS-CoV-2 spike/spike-presenting SApNP vaccine-induced
790 GCs.

791 **fig. S9**. Adjuvant effect on SARS-CoV-2 spike/spike-presenting SApNP vaccine-induced GCs.

792 **fig. S10.** NGS analysis of SARS-CoV-2 spike-specific lymph node (LN) B cells from mice

793 immunized with the spike and SApNP vaccines.

References

1. J. M. Dan *et al.*, Immunological memory to SARS-CoV-2 assessed for up to 8 months after infection. *Science* **371**, eabf4063 (2021).
2. B. Isho *et al.*, Persistence of serum and saliva antibody responses to SARS-CoV-2 spike antigens in COVID-19 patients. *Sci. Immunol.* **5**, eabe5511 (2020).
3. A. S. Iyer *et al.*, Persistence and decay of human antibody responses to the receptor binding domain of SARS-CoV-2 spike protein in COVID-19 patients. *Sci. Immunol.* **5**, eabe0367 (2020).
4. Y. Chen *et al.*, Quick COVID-19 healers sustain anti-SARS-CoV-2 antibody production. *Cell* **183**, 1496-1507.e1416 (2020).
5. S. Marot *et al.*, Rapid decline of neutralizing antibodies against SARS-CoV-2 among infected healthcare workers. *Nat. Commun.* **12**, 844 (2021).
6. R. Burioni, E. J. Topol, Assessing the human immune response to SARS-CoV-2 variants. *Nat. Med.*, Published Ahead-of-Print (2021).
7. H. Tegally *et al.*, Emergence of a SARS-CoV-2 variant of concern with mutations in spike glycoprotein. *Nature*, Published Ahead-of-Print (2021).
8. R. Challen *et al.*, Risk of mortality in patients infected with SARS-CoV-2 variant of concern 202012/1: matched cohort study. *BMJ* **372**, n579 (2021).
9. T. Kirby, New variant of SARS-CoV-2 in UK causes surge of COVID-19. *Lancet Respir. Med.* **9**, e20-e21 (2021).
10. N. G. Davies *et al.*, Estimated transmissibility and impact of SARS-CoV-2 lineage B.1.1.7 in England. *Science*, eabg3055 (2021).
11. N. L. Washington *et al.*, Genomic epidemiology identifies emergence and rapid transmission of SARS-CoV-2 B.1.1.7 in the United States. *medRxiv*, 2021.2002.2006.21251159 (2021).
12. E. C. Sabino *et al.*, Resurgence of COVID-19 in Manaus, Brazil, despite high seroprevalence. *Lancet* **397**, 452-455 (2021).
13. N. R. Faria *et al.*, Genomics and epidemiology of a novel SARS-CoV-2 lineage in Manaus, Brazil. *medRxiv*, 2021.2002.2026.21252554 (2021).
14. J. R. Mascola, B. S. Graham, A. S. Fauci, SARS-CoV-2 viral variants—tackling a moving target. *JAMA*, Published Ahead-of-Print (2021).
15. S. Cherian *et al.*, Convergent evolution of SARS-CoV-2 spike mutations, L452R, E484Q and P681R, in the second wave of COVID-19 in Maharashtra, India. *bioRxiv*, 2021.2004.2022.440932 (2021).
16. C. Zimmer, J. Corum, W. S.-L., in *Coronavirus vaccine tracker*. (https://www.nytimes.com/interactive/2020/science/coronavirus-vaccine-tracker.html).
17. N. Dagan *et al.*, BNT162b2 mRNA Covid-19 vaccine in a nationwide mass vaccination setting. *N. Engl. J. Med.*, Published Ahead-of-Print (2021).
18. L. R. Baden *et al.*, Efficacy and safety of the mRNA-1273 SARS-CoV-2 vaccine. *N. Engl. J. Med.* **384**, 403-416 (2020).
19. T. C. Williams, W. A. Burgers, SARS-CoV-2 evolution and vaccines: cause for concern? *Lancet Respir. Med.*, Published Ahead-of-Print (2021).
20. D. Y. Logunov *et al.*, Safety and efficacy of an rAd26 and rAd5 vector-based heterologous prime-boost COVID-19 vaccine: an interim analysis of a randomised controlled phase 3 trial in Russia. *Lancet* **397**, 671-681 (2021).

21. F. P. Polack *et al.*, Safety and efficacy of the BNT162b2 mRNA Covid-19 vaccine. *N. Engl. J. Med.* **383**, 2603-2615 (2020).
22. Q. Li *et al.*, The impact of mutations in SARS-CoV-2 spike on viral infectivity and antigenicity. *Cell* **182**, 1284-1294.e1289 (2020).
23. C. Rees-Spear *et al.*, The impact of spike mutations on SARS-CoV-2 neutralization. *bioRxiv*, 2021.2001.2015.426849 (2021).
24. C. K. Wibmer *et al.*, SARS-CoV-2 501Y.V2 escapes neutralization by South African COVID-19 donor plasma. *bioRxiv*, 2021.2001.2018.427166 (2021).
25. D. R. Burton, E. J. Topol, Variant-proof vaccines - invest now for the next pandemic. *Nature* **590**, 386-388 (2021).
26. M. Voysey *et al.*, Safety and efficacy of the ChAdOx1 nCoV-19 vaccine (AZD1222) against SARS-CoV-2: an interim analysis of four randomised controlled trials in Brazil, South Africa, and the UK. *Lancet* **397**, 99-111 (2021).
27. E. Andreano *et al.*, SARS-CoV-2 escape in vitro from a highly neutralizing COVID-19 convalescent plasma. *bioRxiv*, 2020.2012.2028.424451 (2020).
28. M. Hoffmann *et al.*, SARS-CoV-2 variants B.1.351 and P.1 escape from neutralizing antibodies. *Cell*, Published Ahead-of-Print (2021).
29. W. F. Garcia-Beltran *et al.*, Multiple SARS-CoV-2 variants escape neutralization by vaccine-induced humoral immunity. *Cell*, Published Ahead-of-Print (2021).
30. P. Wang *et al.*, Antibody resistance of SARS-CoV-2 variants B.1.351 and B.1.1.7. *bioRxiv*, 2021.2001.2025.428137 (2021).
31. P. Supasa *et al.*, Reduced neutralization of SARS-CoV-2 B.1.1.7 variant by convalescent and vaccine sera. *Cell*, Published Ahead-of-Print (2021).
32. D. A. Collier *et al.*, SARS-CoV-2 B.1.1.7 sensitivity to mRNA vaccine-elicited, convalescent and monoclonal antibodies. *medRxiv*, 2021.2001.2019.21249840 (2021).
33. Z. Wang *et al.*, mRNA vaccine-elicited antibodies to SARS-CoV-2 and circulating variants. *Nature*, Published Ahead-of-Print (2021).
34. Q. Li *et al.*, No higher infectivity but immune escape of SARS-CoV-2 501Y.V2 variants. *Cell*, Published Ahead-of-Print (2021).
35. A. Singh, Eliciting B cell immunity against infectious diseases using nanovaccines. *Nat. Nanotechnol.* **16**, 16-24 (2021).
36. G. D. Victora, M. C. Nussenzweig, Germinal centers. *Annu. Rev. Immunol.* **30**, 429-457 (2012).
37. R. Rappuoli, Glycoconjugate vaccines: principles and mechanisms. *Sci. Transl. Med.* **10**, eaat4615 (2018).
38. J. G. Cyster, C. D. C. Allen, B cell responses: cell interaction dynamics and decisions. *Cell* **177**, 524-540 (2019).
39. M. McHeyzer-Williams, S. Okitsu, N. Wang, L. McHeyzer-Williams, Molecular programming of B cell memory. *Nat. Rev. Immunol.* **12**, 24-34 (2012).
40. M. Akkaya, K. Kwak, S. K. Pierce, B cell memory: building two walls of protection against pathogens. *Nat. Rev. Immunol.* **20**, 229-238 (2020).
41. N. S. De Silva, U. Klein, Dynamics of B cells in germinal centres. *Nat. Rev. Immunol.* **15**, 137-148 (2015).
42. O. Bannard, J. G. Cyster, Germinal centers: programmed for affinity maturation and antibody diversification. *Curr. Opin. Immunol.* **45**, 21-30 (2017).

43. P. A. Robert, A. L. J. Marschall, M. Meyer-Hermann, Induction of broadly neutralizing antibodies in germinal centre simulations. *Curr. Opin. Biotechnol.* **51**, 137-145 (2018).
44. H. H. Tam *et al.*, Sustained antigen availability during germinal center initiation enhances antibody responses to vaccination. *Proc. Natl. Acad. Sci. U.S.A.* **113**, E6639-E6648 (2016).
45. K. M. Cirelli *et al.*, Slow delivery immunization enhances HIV neutralizing antibody and germinal center responses via modulation of immunodominance. *Cell* **177**, 1153-1171.e1128 (2019).
46. D. R. Burton, L. Hangartner, Broadly neutralizing antibodies to HIV and their role in vaccine design. *Annu. Rev. Immunol.* **34**, 635-659 (2016).
47. L. He *et al.*, Single-component, self-assembling, protien nanoparticles presenting the receptor binding domain and stabilized spike as SARS-CoV-2 vaccine candidates. *Sci. Adv.* **7**, eabf1591 (2021).
48. D. Wrapp *et al.*, Cryo-EM structure of the 2019-nCoV spike in the prefusion conformation. *Science* **367**, 1260-1263 (2020).
49. K. H. D. Crawford *et al.*, Protocol and reagents for pseudotyping lentiviral particles with SARS-CoV-2 spike protein for neutralization assays. *Viruses* **12**, 513 (2020).
50. A. M. Sholukh *et al.*, Evaluation of SARS-CoV-2 neutralization assays for antibody monitoring in natural infection and vaccine trials. *medRxiv*, 2020.2012.2007.20245431 (2020).
51. D. Pinto *et al.*, Cross-neutralization of SARS-CoV-2 by a human monoclonal SARS-CoV antibody. *Nature* **583**, 290-295 (2020).
52. B. Pulendran, R. Ahmed, Translating innate immunity into immunological memory: implications for vaccine development. *Cell* **124**, 849-863 (2006).
53. S. G. Reed, M. T. Orr, C. B. Fox, Key roles of adjuvants in modern vaccines. *Nat. Med.* **19**, 1597-1608 (2013).
54. B. Pulendran, S. A. P, D. T. O'Hagan, Emerging concepts in the science of vaccine adjuvants. *Nat. Rev. Drug Discov.*, Published Ahead-of-Print (2021).
55. P. S. Arunachalam *et al.*, Adjuvanting a subunit COVID-19 vaccine to induce protective immunity. *Nature*, Published Ahead-of-Print (2021).
56. B. Pulendran, R. Ahmed, Immunological mechanisms of vaccination. *Nat. Immunol.* **12**, 509-517 (2011).
57. K. A. Fitzgerald, J. C. Kagan, Toll-like receptors and the control of immunity. *Cell* **180**, 1044-1066 (2020).
58. T. Kawai, S. Akira, The role of pattern-recognition receptors in innate immunity: update on Toll-like receptors. *Nat. Immunol.* **11**, 373-384 (2010).
59. S. P. Kasturi *et al.*, Programming the magnitude and persistence of antibody responses with innate immunity. *Nature* **470**, 543-547 (2011).
60. T. J. Moyer *et al.*, Engineered immunogen binding to alum adjuvant enhances humoral immunity. *Nat. Med.* **26**, 430-440 (2020).
61. T. L. Flach *et al.*, Alum interaction with dendritic cell membrane lipids is essential for its adjuvanticity. *Nat. Med.* **17**, 479-487 (2011).
62. P. J. Hotez, D. B. Corry, U. Strych, M. E. Bottazzi, COVID-19 vaccines: neutralizing antibodies and the alum advantage. *Nat. Rev. Immunol.* **20**, 399-400 (2020).
63. D. T. O'Hagan, G. S. Ott, G. V. Nest, R. Rappuoli, G. D. Giudice, The history of MF59(®) adjuvant: a phoenix that arose from the ashes. *Expert Rev. Vaccines* **12**, 13-30 (2013).

64. R. Cantisani *et al.*, Vaccine adjuvant MF59 promotes retention of unprocessed antigen in lymph node macrophage compartments and follicular dendritic cells. *J. Immunol.* **194**, 1717-1725 (2015).
65. H. Ishikawa, G. N. Barber, STING is an endoplasmic reticulum adaptor that facilitates innate immune signalling. *Nature* **455**, 674-678 (2008).
66. H. Ishikawa, Z. Ma, G. N. Barber, STING regulates intracellular DNA-mediated, type I interferon-dependent innate immunity. *Nature* **461**, 788-792 (2009).
67. G. N. Barber, STING: infection, inflammation and cancer. *Nat. Rev. Immunol.* **15**, 760-770 (2015).
68. B. Guy, The perfect mix: recent progress in adjuvant research. *Nat. Rev. Microbiol.* **5**, 396-397 (2007).
69. M. S. Duthie, H. P. Windish, C. B. Fox, S. G. Reed, Use of defined TLR ligands as adjuvants within human vaccines. *Immunol. Rev.* **239**, 178-196 (2011).
70. M. C. Hanson *et al.*, Nanoparticulate STING agonists are potent lymph node-targeted vaccine adjuvants. *J. Clin. Invest.* **125**, 2532-2546 (2015).
71. M. P. Steinbuck *et al.*, A lymph node–targeted Amphiphile vaccine induces potent cellular and humoral immunity to SARS-CoV-2. *Sci. Adv.* **7**, eabe5819 (2021).
72. D. S. Wilson *et al.*, Antigens reversibly conjugated to a polymeric glyco-adjuvant induce protective humoral and cellular immunity. *Nat. Mater.* **18**, 175-185 (2019).
73. E. Tonti *et al.*, Bisphosphonates target B cells to enhance humoral immune responses. *Cell Rep.* **5**, 323-330 (2013).
74. F. G. Delemarre, N. Kors, N. van Rooijen, The in situ immune response in popliteal lymph nodes of mice after macrophage depletion. Differential effects of macrophages on thymus-dependent and thymus-independent immune responses. *Immunobiology* **180**, 395-404 (1990).
75. Y.-N. Zhang, W. Poon, E. Sefton, W. C. W. Chan, Suppressing subcapsular sinus macrophages enhances transport of nanovaccines to lymph node follicles for robust humoral immunity. *ACS Nano* **14**, 9478-9490 (2020).
76. J. G. Liang *et al.*, S-Trimer, a COVID-19 subunit vaccine candidate, induces protective immunity in nonhuman primates. *Nat. Commun.* **12**, 1346 (2021).
77. P. Richmond *et al.*, Safety and immunogenicity of S-Trimer (SCB-2019), a protein subunit vaccine candidate for COVID-19 in healthy adults: a phase 1, randomised, double-blind, placebo-controlled trial. *Lancet* **397**, 682-694 (2021).
78. E. S. Rosenberg *et al.*, Vigorous HIV-1-specific CD4+ T cell responses associated with control of viremia. *Science* **278**, 1447-1450 (1997).
79. L. M. Snell *et al.*, Overcoming CD4 Th1 cell fate restrictions to sustain antiviral CD8 T cells and control persistent virus infection. *Cell Rep.* **16**, 3286-3296 (2016).
80. J. Zhu, H. Yamane, W. E. Paul, Differentiation of effector CD4 T cell populations (*). *Annu. Rev. Immunol.* **28**, 445-489 (2010).
81. S. Kumar *et al.*, Neutralizing antibodies induced by first-generation gp41-stabilized HIV-1 envelope trimers and nanoparticles. *bioRxiv*, 2020.2012.2002.408328 (2020).
82. R. Shi *et al.*, A human neutralizing antibody targets the receptor-binding site of SARS-CoV-2. *Nature* **584**, 120-124 (2020).
83. T. F. Rogers *et al.*, Isolation of potent SARS-CoV-2 neutralizing antibodies and protection from disease in a small animal model. *Science* **369**, 956-963 (2020).

84. C. D. Morris *et al.*, Differential antibody responses to conserved HIV-1 neutralizing epitopes in the context of multivalent scaffolds and native-like gp140 trimers. *mBio* **8**, e00036-00017 (2017).
85. F. Chen *et al.*, Functional convergence of a germline-encoded neutralizing antibody response in rhesus macaques immunized with HCV envelope glycoproteins. *Immunity* **54**, 781-796.e784 (2021).
86. G. P. Wen *et al.*, Quantitative evaluation of protective antibody response induced by hepatitis E vaccine in humans. *Nat. Commun.* **11**, 3971 (2020).
87. B. Ju *et al.*, Human neutralizing antibodies elicited by SARS-CoV-2 infection. *Nature* **584**, 115-119 (2020).
88. Y.-N. Zhang *et al.*, Nanoparticle size influences antigen retention and presentation in lymph node follicles for humoral immunity. *Nano Lett.* **19**, 7226-7235 (2019).
89. K. M. Cirelli, S. Crotty, Germinal center enhancement by extended antigen availability. *Curr. Opin. Immunol.* **47**, 64-69 (2017).
90. B. A. Heesters, R. C. Myers, M. C. Carroll, Follicular dendritic cells: dynamic antigen libraries. *Nat. Rev. Immunol.* **14**, 495-504 (2014).
91. J. G. Cyster, B cell follicles and antigen encounters of the third kind. *Nat. Immunol.* **11**, 989-996 (2010).
92. F. D. Batista, N. E. Harwood, The who, how and where of antigen presentation to B cells. *Nat. Rev. Immunol.* **9**, 15-27 (2009).
93. M. Kuka, M. Iannacone, Viral subversion of B cell responses within secondary lymphoid organs. *Nat. Rev. Immunol.* **18**, 255-265 (2018).
94. R. Rappuoli, D. Serruto, Self-assembling nanoparticles usher in a new era of vaccine design. *Cell* **176**, 1245-1247 (2019).
95. C. D. C. Allen, T. Okada, J. G. Cyster, Germinal-center organization and cellular dynamics. *Immunity* **27**, 190-202 (2007).
96. C. D. C. Allen, J. G. Cyster, Follicular dendritic cell networks of primary follicles and germinal centers: Phenotype and function. *Semin. Immunol.* **20**, 14-25 (2008).
97. L. Mesin, J. Ersching, Gabriel D. Victora, Germinal center B cell dynamics. *Immunity* **45**, 471-482 (2016).
98. N. Baumgarth, The shaping of a B cell pool maximally responsive to infections. *Annu. Rev. Immunol.* **39**, (2021).
99. J. López-Sagaseta, E. Malito, R. Rappuoli, M. J. Bottomley, Self-assembling protein nanoparticles in the design of vaccines. *Comput. Struct. Biotechnol. J.* **14**, 58-68 (2016).
100. D. J. Irvine, M. C. Hanson, K. Rakhra, T. Tokatlian, Synthetic nanoparticles for vaccines and immunotherapy. *Chem. Rev.* **115**, 11109-11146 (2015).
101. D. J. Irvine, M. A. Swartz, G. L. Szeto, Engineering synthetic vaccines using cues from natural immunity. *Nat. Mater.* **12**, 978-990 (2013).
102. Y. Kato *et al.*, Multifaceted effects of antigen valency on B cell response composition and differentiation in vivo. *Immunity* **53**, 548-563.e548 (2020).
103. S. Crotty, Follicular helper CD4 T cells (TFH). *Annu. Rev. Immunol.* **29**, 621-663 (2011).
104. A K Szakal, a. M H Kosco, J. G. Tew, Microanatomy of lymphoid tissue during humoral immune responses: structure function relationships. *Annu. Rev. Immunol.* **7**, 91-109 (1989).
105. J. Merkenschlager *et al.*, Dynamic regulation of TFH selection during the germinal centre reaction. *Nature* **591**, 458-463 (2021).

106. Z. Shulman *et al.*, T follicular helper cell dynamics in germinal centers. *Science* **341**, 673-677 (2013).
107. C. Viant *et al.*, Antibody affinity shapes the choice between memory and germinal center B cell fates. *Cell* **183**, 1298-1311.e1211 (2020).
108. K. Lederer *et al.*, SARS-CoV-2 mRNA vaccines foster potent antigen-specific germinal center responses associated with neutralizing antibody generation. *Immunity* **53**, 1281-1295.e1285 (2020).
109. G. S. Shukla, Y. J. Sun, S. C. Pero, G. S. Sholler, D. N. Krag, Immunization with tumor neoantigens displayed on T7 phage nanoparticles elicits plasma antibody and vaccine-draining lymph node B cell responses. *J. Immunol. Methods* **460**, 51-62 (2018).
110. L. He *et al.*, Proof of concept for rational design of hepatitis C virus E2 core nanoparticle vaccines. *Sci. Adv.* **6**, eaaz6225 (2020).
111. A. A. Cohen *et al.*, Mosaic nanoparticles elicit cross-reactive immune responses to zoonotic coronaviruses in mice. *Science* **371**, 735-741 (2021).
112. A. C. Walls *et al.*, Elicitation of broadly protective sarbecovirus immunity by receptor-binding domain nanoparticle vaccines. *bioRxiv*, 2021.2003.2015.435528 (2021).
113. R. Rappuoli *et al.*, Vaccinology in the post−COVID-19 era. *Proc. Natl. Acad. Sci. U.S.A.* **118**, e2020368118 (2021).
114. M. Jeyanathan *et al.*, Immunological considerations for COVID-19 vaccine strategies. *Nat. Rev. Immunol.* **20**, 615-632 (2020).
115. L. Corey, J. R. Mascola, A. S. Fauci, F. S. Collins, A strategic approach to COVID-19 vaccine R&D. *Science* **368**, 948-950 (2020).
116. L. DeFrancesco, Whither COVID-19 vaccines? *Nat. Biotechnol.* **38**, 1132-1145 (2020).
117. C. Keech *et al.*, Phase 1–2 trial of a SARS-CoV-2 recombinant spike protein nanoparticle vaccine. *N. Engl. J. Med.* **383**, 2320-2332 (2020).
118. T. Tokatlian *et al.*, Innate immune recognition of glycans targets HIV nanoparticle immunogens to germinal centers. *Science* **363**, 649-654 (2019).
119. S. N. Mueller, S. Tian, J. M. DeSimone, Rapid and persistent delivery of antigen by lymph node targeting PRINT nanoparticle vaccine carrier to promote humoral immunity. *Mol. Pharm.* **12**, 1356-1365 (2015).
120. B. Zhang *et al.*, A platform incorporating trimeric antigens into self-assembling nanoparticles reveals SARS-CoV-2-spike nanoparticles to elicit substantially higher neutralizing responses than spike alone. *Sci. Rep.* **10**, 18149 (2020).
121. A. C. Walls *et al.*, Elicitation of potent neutralizing antibody responses by designed protein nanoparticle vaccines for SARS-CoV-2. *Cell* **183**, 1367-1382.e1317 (2020).
122. A. E. Powell *et al.*, A single immunization with spike-functionalized ferritin vaccines elicits neutralizing antibody responses against SARS-CoV-2 in mice. *ACS Cent. Sci.* **7**, 183-199 (2021).
123. P. J. M. Brouwer *et al.*, Two-component spike nanoparticle vaccine protects macaques from SARS-CoV-2 infection. *Cell* **184**, 1188-1200.e1119 (2021).
124. K. S. Park *et al.*, Lipid-based vaccine nanoparticles for induction of humoral immune responses against HIV-1 and SARS-CoV-2. *J. Control. Release* **330**, 529-539 (2021).
125. Y.-F. Kang *et al.*, Rapid development of SARS-CoV-2 spike protein receptor-binding domain self-assembled nanoparticle vaccine candidates. *ACS Nano* **15**, 2738-2752 (2021).

126. J. H. Lam *et al.*, Next generation vaccine platform: polymersomes as stable nanocarriers for a highly immunogenic and durable SARS-CoV-2 spike protein subunit vaccine. *bioRxiv*, 2021.2001.2024.427729 (2021).
127. W. C. Huang *et al.*, SARS-CoV-2 RBD neutralizing antibody induction is enhanced by particulate vaccination. *Adv. Mater.* **32**, e2005637 (2020).
128. T. K. Tan *et al.*, A COVID-19 vaccine candidate using SpyCatcher multimerization of the SARS-CoV-2 spike protein receptor-binding domain induces potent neutralising antibody responses. *Nat. Commun.* **12**, 542 (2021).
129. D. Lainšček *et al.*, Immune response to vaccine candidates based on different types of nanoscaffolded RBD domain of the SARS-CoV-2 spike protein. *bioRxiv*, 2020.2008.2028.244269 (2020).
130. X. Ma *et al.*, Nanoparticle vaccines based on the receptor binding domain (RBD) and heptad repeat (HR) of SARS-CoV-2 elicit robust protective immune responses. *Immunity* **53**, 1315-1330.e1319 (2020).
131. N. C. Dalvie *et al.*, Engineered SARS-CoV-2 receptor binding domain improves immunogenicity in mice and elicits protective immunity in hamsters. *bioRxiv*, 2021.2003.2003.433558 (2021).
132. I. Quast, D. Tarlinton, B cell memory: understanding COVID-19. *Immunity* **54**, 205-210 (2021).
133. D. J. Irvine, B. J. Read, Shaping humoral immunity to vaccines through antigen-displaying nanoparticles. *Curr. Opin. Immunol.* **65**, 1-6 (2020).
134. M. D. Shin *et al.*, COVID-19 vaccine development and a potential nanomaterial path forward. *Nat. Nanotechnol.* **15**, 646-655 (2020).
135. L. He *et al.*, Single-component multilayered self-assembling nanoparticles presenting rationally designed glycoprotein trimers as Ebola virus vaccines. *bioRxiv*, 2020.2008.2022.262634 (2020).
136. L. He *et al.*, HIV-1 vaccine design through minimizing envelope metastability. *Sci. Adv.* **4**, aau6769 (2018).
137. L. Wijaya *et al.*, An accelerated rabies vaccine schedule based on toll-like receptor 3 (TLR3) agonist PIKA adjuvant augments rabies virus specific antibody and T cell response in healthy adult volunteers. *Vaccine* **35**, 1175-1183 (2017).
138. C. A. Schneider, W. S. Rasband, K. W. Eliceiri, NIH Image to ImageJ: 25 years of image analysis. *Nat. Methods* **9**, 671-675 (2012).
139. T. J. Johnson, Glutaraldehyde fixation chemistry: oxygen-consuming reactions. *Eur. J. Cell Biol.* **45**, 160-169 (1987).
140. K. Mochizuki *et al.*, Programming of donor T cells using allogeneic δ-like ligand 4-positive dendritic cells to reduce GVHD in mice. *Blood* **127**, 3270-3280 (2016).
141. T. Tiller, C. E. Busse, H. Wardemann, Cloning and expression of murine Ig genes from single B cells. *J. Immunol. Methods* **350**, 183-193 (2009).

Acknowledgements

Funding: This work was funded by National Institutes of Health grants AI137472, AI139092 (to J.Z.), Ufovax/SFP-2018-0416, Ufovax/SFP-2018-1013, and Ufovax/SFP-2020-0111 (to J.Z.). Y.-

N.Z. thanks the Natural Sciences and Engineering Research Council of Canada (NSERC) for a postdoctoral fellowship. We thank V. Bradaschia, K. Duffin, and M. Ganguly at the Centre for Phenogenomics for their expertise in histology and immunostaining. We acknowledge the expert assistance of S. Henderson, K. Vanderpool, and T. Fassel at the Core Microscopy Facility at The Scripps Research Institute. We thank A. Saluk, B. Seegers, and B. Monteverde at the Flow Cytometry Core Facility of The Scripps Research Institute for their expertise in flow cytometry. The authors thank M. Arends for proofreading the manuscript. **Author contributions:** Project design by Y.-N.Z., L.H., and J.Z. SARS-CoV-2 variant plasmid design and processing by L.H. and C.S. Antigen production, purification, and basic characterization by T.N., T.F., and L.H. Antibody and mouse plasma neutralization by J.P., T.F., and L.H. Mouse immunization, plasma collection, and lymph node isolation by Y.-N.Z. Vaccine-induced T-cell response analysis by Y.W., C.A., and Y.Z. B cell sorting, antibody cloning, and synthesis by C.S. and L.H. Antibody expression, purification, and ELISA by C.S. and T.N. NGS and bioinformatics by L.H. and J.Z. Immunohistology, TEM, and flow cytometry by Y.-N.Z. Manuscript written by Y.-N.Z., Y.Z., L.H., and J.Z. All authors commented on the manuscript. This is manuscript number 30082 from The Scripps Research Institute. **Competing interests:** The authors declare no competing interests. **Data and material availability:** All data are available in the main text or in the supplementary materials. Additional data related to this paper may be requested from the corresponding author.

Figure Legends

Fig. 1. SARS-CoV-2 SApNP vaccines induce broadly neutralizing plasma responses to three variants of concern. (**A**) Molecular surface representations of vaccine constructs, including two spikes ($S2P_{ECTO}$-5GS-1TD0 and S2GΔHR2-5GS-1TD0) and three spike-presenting SApNPs (S2GΔHR2-5GS-ferritin (FR), S2GΔHR2-5GS-E2p-LD4-PADRE (E2p-L4P), and S2GΔHR2-10GS-I3-01v9-LD7-PADRE (I3-01v9-L7P)). Representative negative-stain EM (nsEM) image of S2GΔHR2-10GS- I3-01v9-L7P SApNPs is shown on the right. (**B**) Neutralization of the original Wuhan-Hu-1 strain by mouse plasma induced by five different vaccines at week 5 after two intraperitoneal injections. ID_{50} titers derived from SARS-CoV-2-pp neutralization assays are plotted, with average ID_{50} values labeled on the plots. (**C**) Mouse plasma neutralization against the original Wuhan-Hu-1 strain and three variants, B.1.1.7, B1.351, and P.1, at week 5 after two intraperitoneal injections of the adjuvanted S2GΔHR2-10GS-I3-01v9-L7P vaccine. Left panels 1-4: percent neutralization plots of individual mice against 4 SARS-CoV-2 strains; Right panel: ID_{50} plot. In (B) and (C), the plasma samples were generated in our previous study (*47*), in which mice were immunized with 50 μg of adjuvanted vaccine antigen. (**D**) Neutralization of the original Wuhan-Hu-1 strain by mouse plasma induced the S2GΔHR2 spike and two large S2GΔHR2-presenting SApNPs. Vaccines were administered via footpad injections (0.8 μg/injection, for a total of 3.3 μg/mouse). **(E)** Mouse plasma neutralization against the original Wuhan-Hu-1 strain and three variants, B.1.1.7, B1.351, and P.1, at week 5 after two footpad injections of the S2GΔHR2 spike and two large S2GΔHR2-presenting SApNPs. In (B)-(E), the ID_{50} values are plotted as mean ± SEM. The data were analyzed using two-tailed unpaired Student's *t*-test for comparison between different vaccine groups or two-tailed paired Student's *t*-test for comparison of ID_{50} titers against SARS-Cov-2 variants using the same plasma samples from a mouse. *p <

0.05, $**p < 0.01$. (**F**) Neutralization of four SARS-CoV-2 strains by human monoclonal antibodies including CR3022, B38, CB6, S309, CC12.1, CC12.3, C105, and P2B-2F6. IC_{50} values are listed and color-coded (white: IC_{50} > 10 μg/ml; green to red: low to high). The IC_{50} values were calculated with the % neutralization range constrained within 0.0-100.0%.

Fig. 2. Adjuvants enhance the I3-01v9 SApNP vaccine -induced plasma neuralization of both the wildtype strain and three variants of concern. (A) Schematic representation of mouse immunization with the I3-01v9 SApNP with diverse adjuvant formulations and functional assessment by SARS-CoV-2-pp neutralization assays and T-cell analysis. Conventional adjuvants, STING/TLR agonists, macrophage inhibitors, and adjuvant combinations were compared to non-adjuvanted control (PBS). (**B, C**) Mouse plasma neutralization against the wildtype SARS-CoV-2 strain, Wuhan-Hu-1, at weeks 5 and 8 after two and three footpad injections, respectively. ID_{50} titers derived from SARS-CoV-2-pp neutralization assays are plotted, with average ID_{50} values labeled on the plots. (**D**) Neutralization against three SARS-CoV-2 variants by mouse plasma from STING (top panel) and CpG (bottom panel)-formulated vaccine groups. ID_{50} titers derived from SARS-CoV-2-pp neutralization assays are plotted. Splenic mononuclear cells derived from mice in the STING and CpG groups (n=5/group) at week 8 were cultured in the presence of BALB/C DCs pulsed with I3-01v9 SApNP ($1x10^{-7}$ mM). Cells were harvested 16 hours following re-activation. (**E**) Production of IFN-γ-producing Th1 $CD4^+$ T cells and IL-4-producing Th2 $CD4^+$ T cells. (**F**) IFN-γ-producing $CD8^+$ effector T cells. The P values were determined by one-way ANOVA. *, P<0.05; **, P<0.01; ***, P<0.001.

Fig. 3. Single-cell isolation identifies vaccine-elicited mouse neutralizing antibody lineages with diverse breadth and potency. (**A**) Genetic analysis of 20 mouse antibodies identified from

M2 in the RBD-5GS-1TD0 trimer group (4), M4 in the S2GΔHR2-5GS-1TD0 spike group (6), and M2 in the S2GΔHR2-10GS-I3-01v9-L7P SApNP group (10). Antibodies isolated by the RBD and spike probes are highlighted in light gray and orange shade, respectively. (**B**) Neutralization of four SARS-CoV-2 strains by 10 RBD and spike-elicited mouse antibodies (left) and 10 SApNP-elicited mouse antibodies (right). IC_{50} values are listed and color-coded (white: IC_{50} > 100 μg/ml; green to red: low to high). The IC_{50} values were calculated with the %neutralization range constrained within 0.0-100.0%. (**C**) EC_{50} (μg/ml) values of 20 mouse antibodies binding to the two SARS-CoV-2 antigens, the RBD monomer and S2GΔHR2-5GS-1TD0 spike, both with the Wuhuan-Hu-1 backbone. Antigen binding was measured by ELISA in duplicates, with mean value and standard deviation (SD) shown as black and red lines, respectively. (**D**) Divergence-identity analysis of selected mouse NAbs in the context of RBD/spike-specific splenic B cells. HCs and KCs are plotted as a function of sequence identity to the template and sequence divergence from putative germline genes. Color coding denotes sequence density. The template and sequences identified based on the V gene assignment and a CDR3 identity of 90%/85% or greater to the template are shown as black and orange/magenta dots on the 2D plots, with the number of related sequences labeled accordingly. The 2D plots for other NAbs are shown in fig. S4D-F.

Fig. 4. SARS-CoV-2 SApNP vaccines induce long-term lymph node follicle retention. (**A**, **B**) S2GΔHR2-presenting I3-01v9 SApNP vaccine distribution in a lymph node 12 h after (**A**) a single-dose or (**B**) prime-boost footpad injections (10 μg/injection, 40 μg/mouse). A schematic illustration of SApNPs in lymph node follicles is shown. (**C**, **D**) Histological images of the S2GΔHR2 spike and S2GΔHR2-presenting E2p and I3-01 SApNP vaccine trafficking and retention in lymph node follicles 2 h to 8 weeks after (**C**) a single-dose or (**D**) prime-boost injections, with a scale bar of

50 μm shown for each image. (**E**, **F**) Quantification of vaccine accumulation in lymph node follicles 48 h after (**E**) a single-dose or (**F**) prime-boost injections. Data were collected from more than 10 lymph node follicles (n = 3-4 mice/group). The data points are expressed as mean ± SD. The data were analyzed using one-way ANOVA followed by Tukey's multiple comparison *post hoc* test. $^{**}p < 0.01$, $^{***}p < 0.001$, $^{****}p < 0.0001$.

Fig. 5. SARS-CoV-2 SApNP vaccines interact with follicular dendritic cells (FDCs) and are presented on FDC dendrites to B cells. (**A**, **B**) S2GΔHR2 spike and S2GΔHR2-presenting E2p and I3-01 SApNP vaccine interaction with FDC networks in lymph node follicles 12 h after (**A**) a single-dose or (**B**) prime-boost injections (10 μg/injection, 40 μg/mouse). Vaccine antigens (the S2GΔHR2 spike and S2GΔHR2-presenting E2p and I3-01 SApNPs) colocalized with FDC networks. Immunostaining is color-coded (Green: CD21; Red: CD169; White: anti-spike), with scale bars of 500 μm and 100 μm shown for a complete lymph node and an enlarged image of a follicle, respectively. (**C**) Representative TEM images of an FDC surrounded by multiple B cells. S2GΔHR2-presenting I3-01 SApNPs (yellow arrows) presented on FDC dendrites.

Fig. 6. SARS-CoV-2 SApNP vaccines induce robust long-lived germinal centers. (**A**) Top: Representative immunohistological images of germinal centers at week 2 after a single-dose injection of the S2GΔHR2-presenting I3-01 SApNP vaccine (10 μg/injection, 40 μg/mouse). Bottom: germinal center B cells ($GL7^+$, red) adjacent to FDCs ($CD21^+$, green) in lymph node follicles (left) and T_{fh} cells in the light zone (LZ) of germinal centers (right). Scale bars of 500 μm and 50 μm are shown for a complete lymph node and an enlarged image of a follicle, respectively. (**B**, **C**) Quantification of germinal center reactions using immunofluorescent images: GC/FDC ratio and sizes of germinal centers 2, 5, and 8 weeks after (**B**) a single-dose or (**C**) prime-boost

injections (*n* = 4-7 mice/group). The GC/FDC ratio is defined as whether germinal center formation is associated with an FDC network (%). Representative immunohistological images of germinal centers in mice immunized using S2GΔHR2 spike or S2GΔHR2-presenting E2p and I3-01 SApNP vaccines at week 8 after (**D**) a single-dose or (**E**) prime-boost injections, with a scale bar of 50 μm shown for each image. (**F**, **G**) Quantification of germinal center reactions using flow cytometry: percentage and number of germinal center B cells and T_{fh} cells 2, 5, and 8 weeks after (**F**) a single-dose or (**G**) prime-boost injections. The data points are shown as mean ± SD. The data were analyzed using one-way ANOVA followed by Tukey's multiple comparison *post hoc* test for each timepoint. *$p < 0.05$, **$p < 0.01$, ***$p < 0.001$, ****$p < 0.0001$.

Figure 1

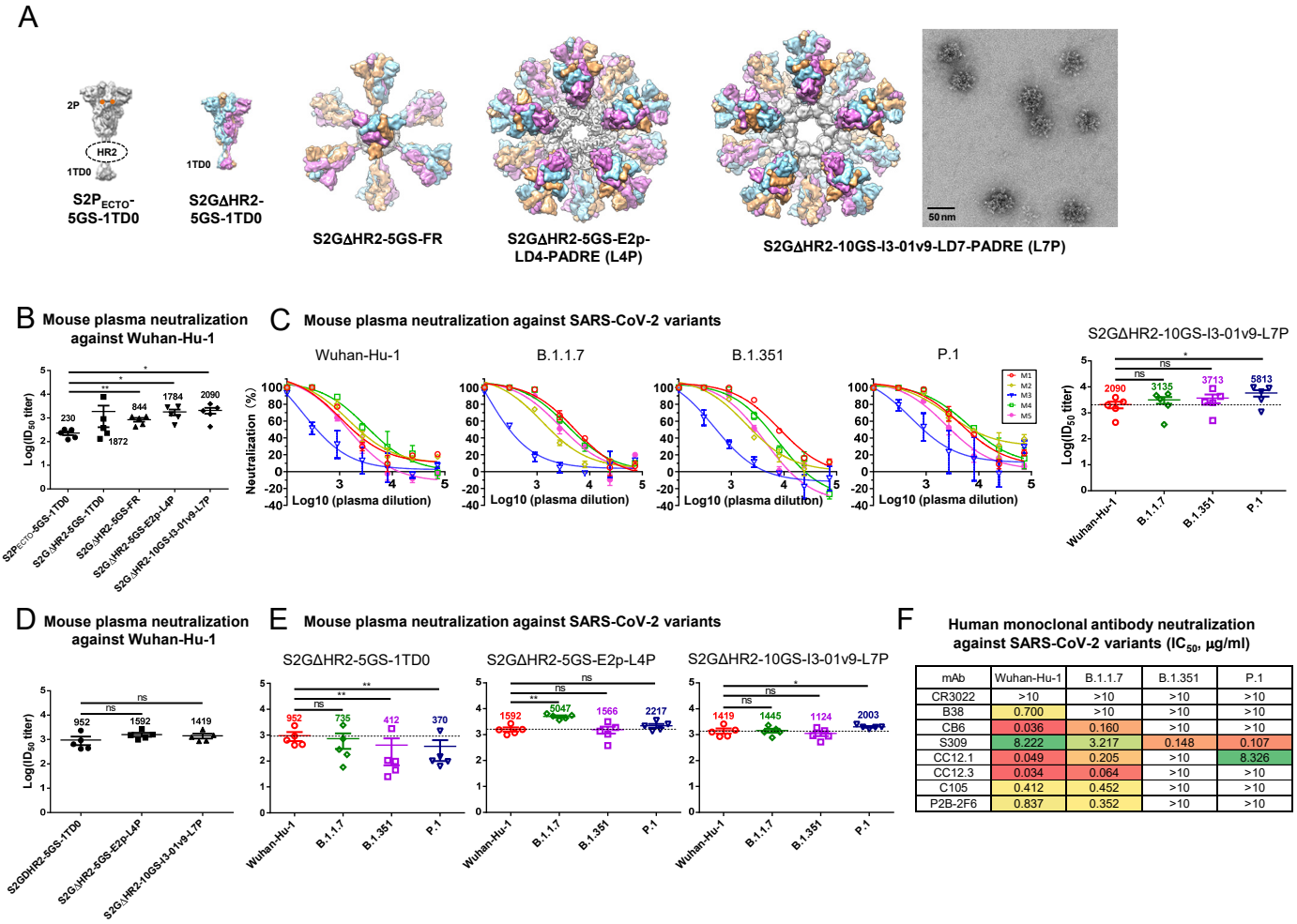

mAb	Wuhan-Hu-1	B.1.1.7	B.1.351	P.1
CR3022	>10	>10	>10	>10
B38	0.700	>10	>10	>10
CB6	0.036	0.160	>10	>10
S309	8.222	3.217	0.148	0.107
CC12.1	0.049	0.205	>10	8.326
CC12.3	0.034	0.064	>10	>10
C105	0.412	0.452	>10	>10
P2B-2F6	0.837	0.352	>10	>10

Figure 2

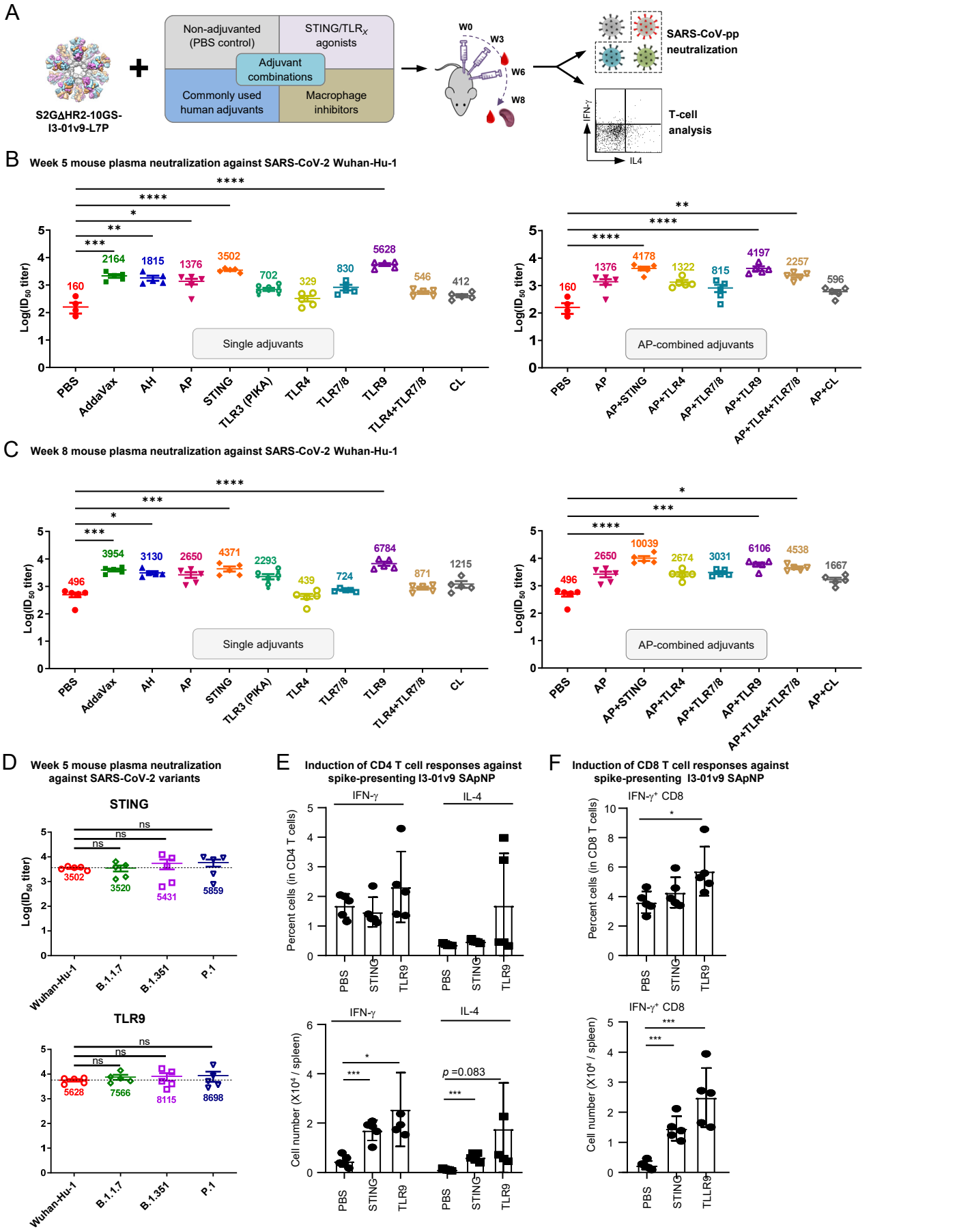

Figure 3

A **Antibodies identified from SARS-CoV-2 RBD, spike, and nanoparticle-immunized mice by single-cell sorting [a]**

Antibody	V_H family [b]	V_H identity [b]	HCDR3 (# aa) [c]	V_K family [b]	V_K identity [b]	KCDR3 (# aa) [c]
TRBD-R-4B6	IGHV2-2*02	97.6%	WGYWYFDV (8)	IGKV8-24*01	98.0%	QQHYSTPLT (9)
TRBD-R-4F3	IGHV1-12*01	95.6%	DDYYALDY (8)	IGKV8-30*01	97.0%	QQYYSYPWT (9)
TRBD-R-4G5	IGHV1-5*01	94.9%	DYYGYGNY (8)	IGKV12-44*01	99.6%	QHHYGTPLT (9)
TRBD-R-5B9	IGHV1S126*01	88.0%	RDYYGNNPFDF (11)	IGKV2-137*01	97.7%	MQHLEYPYT (9)
S2GD-S-1F3	IGHV1-7*01	95.9%	SEYGNLYYAMDY (12)	IGKV3-4*01	97.6%	QQSNEDPLT (9)
S2GD-S-2C10	IGHV1-14*01	98.6%	FTKVEGY (7)	IGKV3-2*01	97.3%	HQSKEVPWT (9)
S2GD-R-1F9	IGHV14-1*02	98.6%	WEGRAMDY (8)	IGKV10-94*01	95.8%	QQYSKLPYT (9)
S2GD-R-2D10	IGHV14-3*02	95.1%	WDNAAYYYGMDY (12)	IGKV14-111*01	95.7%	LQYDELYT (8)
S2GD-R-2E4	IGHV1S81*02	92.8%	YGRYFDC (7)	IGKV14-130*01	98.2%	LQFYEFPYT (9)
S2GD-R-2F4	IGHV1-37*01	95.8%	ERHY (4)	IGKV14-100*01	98.9%	VQYDQFPYT (9)
I3V9-S-1C9	IGHV14-1*02	98.6%	GDFDY (5)	IGKV4-55*01	96.1%	QQWGTYPPRT (10)
I3V9-S-2D8	IGHV14-3*02	95.6%	GLYDYDGSPFAY (12)	IGKV10-96*01	96.8%	QQGNTLPYT (9)
I3V9-S-2D10	IGHV14-1*02	95.5%	GDGNY (5)	IGKV4-57*01	97.8%	QQRSSYPIFT (10)
I3V9-R-1G3	IGHV1S81*02	94.2%	DGSSAY (6)	IGKV9-120*01	97.1%	LQYAGSPFT (9)
I3V9-R-1G9	IGHV1-18*01	93.2%	DGYPYYYAMDY (11)	IGKV6-15*01	97.9%	QQYNSYPWT (9)
I3V9-R-1F5	IGHV1-82*01	92.5%	SWDGLVFAY (9)	IGKV4-55*01	93.3%	QQWNNFPPT (9)
I3V9-R-2E11	IGHV1S81*02	92.2%	DGSIAY (6)	IGKV9-120*01	98.5%	LQYASSPYT (9)
I3V9-R-2F2	IGHV1-18*01	89.4%	DRYDRYFDV (9)	IGKV4-55*01	92.9%	QQWNNFPPT (9)
I3V9-R-2F5	IGHV1-20*02	96.2%	SHDYPFDY (8)	IGKV9-123*01	97.5%	LQRNAYPYT (9)
I3V9-R-2F10	IGHV1-18*01	92.9%	DGYPYYYALDY (11)	IGKV12-98*01	97.6%	QQLYSTPLT (9)

[a] Splenic B cells from three mice immunized with the RBD-5GS-1TD0 trimer, S2GΔHR2-5GS-1TD0 spike, and S2GΔHR2-10GS-I3-01v9-L7P NP were sorted to isolate monoclonal neutralizing antibodies. Antibodies are named as [vaccine]-[probe]-[sorting index]. [vaccine]: TRBD, S2GD, and I3V9 stand for RBD-5GS-1TD0, S2GΔHR2-5GS-1TD0, and S2GΔHR2-10GS-I3-01v9-L7P, respectively. [probe]: R and S stand for RBD-5GS-foldon-Avi-Biot and S2GΔHR2-5GS-foldon-Avi-Biot, respectively. Spike and RBD-sorted antibodies are highlighted in light gray and light brown shade, respectively.
[b] $V_{H/K}$ gene assignment and identity were determined by IGBLAST (https://www.ncbi.nlm.nih.gov/igblast/).
[c] H/KCDR3 sequence and length are determined following the Kabat numbering scheme.

B **RBD and spike-elicited mouse neutralizing antibodies against SARS-CoV-2 wildtype and variants (IC_{50}, μg/ml)**

	Antibody	Wuhan-Hu-1	B.1.1.7	B.1.351	P.1
RBD	TRBD-R-4B6	0.109	0.053	>100	>100
	TRBD-R-4F3	4.074	6.217	0.126	0.085
	TRBD-R-4G5	0.019	0.031	1.157	0.823
	TRBD-R-5B9	1.003	2.529	1.447	0.693
Spike	S2GD-S-1F3	0.273	24.130	>100	>100
	S2GD-S-2C10	0.030	0.020	0.906	1.175
	S2GD-R-1F9	1.199	0.941	4.015	2.719
	S2GD-R-2D10	16.970	3.622	14.430	1.502
	S2GD-R-2E4	2.598	1.868	0.236	0.162
	S2GD-R-2F4	1.921	1.132	3.673	3.867

Spike nanoparticle-elicited mouse neutralizing antibodies against SARS-CoV-2 wildtype and variants (IC_{50}, μg/ml)

	Antibody	Wuhan-Hu-1	B.1.1.7	B.1.351	P.1
I3-01v9 SApNP	I3V9-S-1C9	0.120	0.089	0.053	0.074
	I3V9-S-2D8	>100	2.634	11.820	6.471
	I3V9-S-2D10	0.095	0.051	0.102	0.181
	I3V9-R-1F5	9.291	3.083	6.241	3.101
	I3V9-R-1G3	0.027	0.026	10.430	9.309
	I3V9-R-1G9	0.024	0.008	0.012	0.007
	I3V9-R-2E11	0.152	0.052	>100	>100
	I3V9-R-2F2	3.598	14.350	3.167	1.583
	I3V9-R-2F5	2.582	3.659	3.759	8.757
	I3V9-R-2F10	54.520	>100	14.100	11.740

C **Mouse neutralizing antibodies binding to RBD and spike antigens**

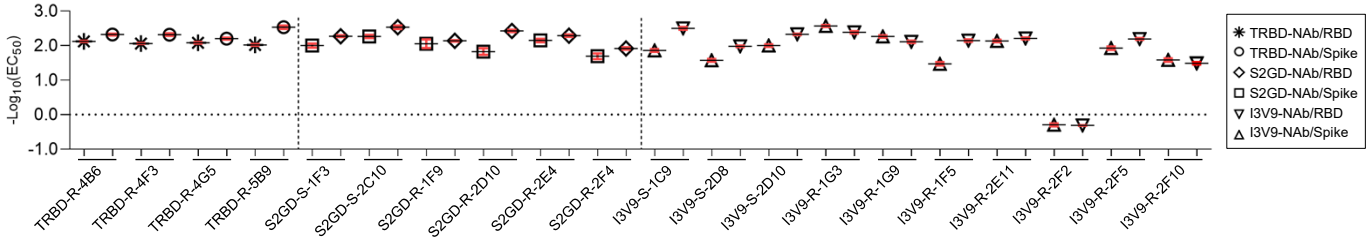

D

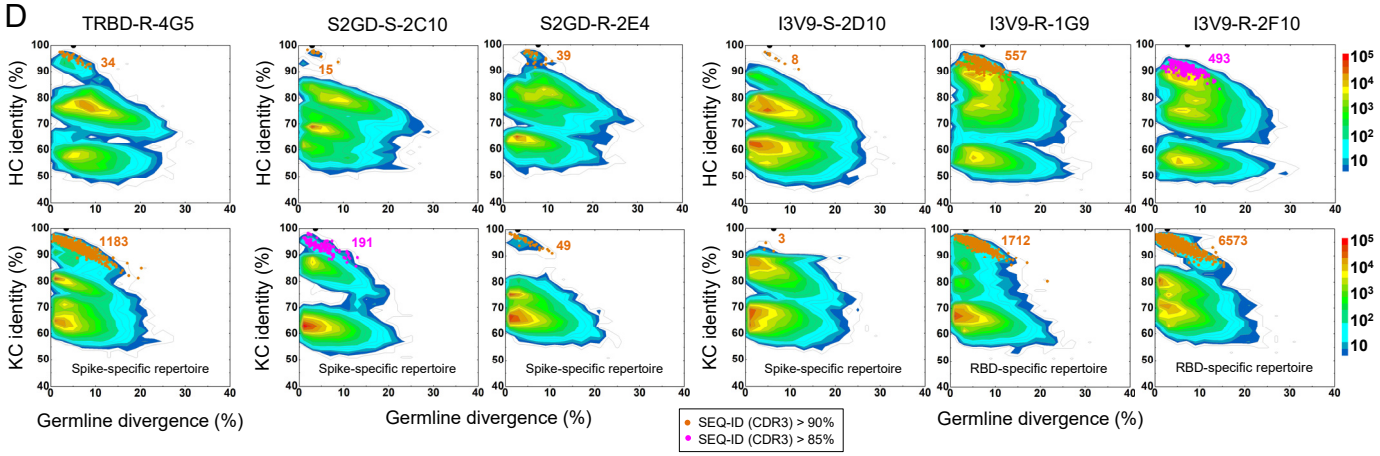

Figure 4

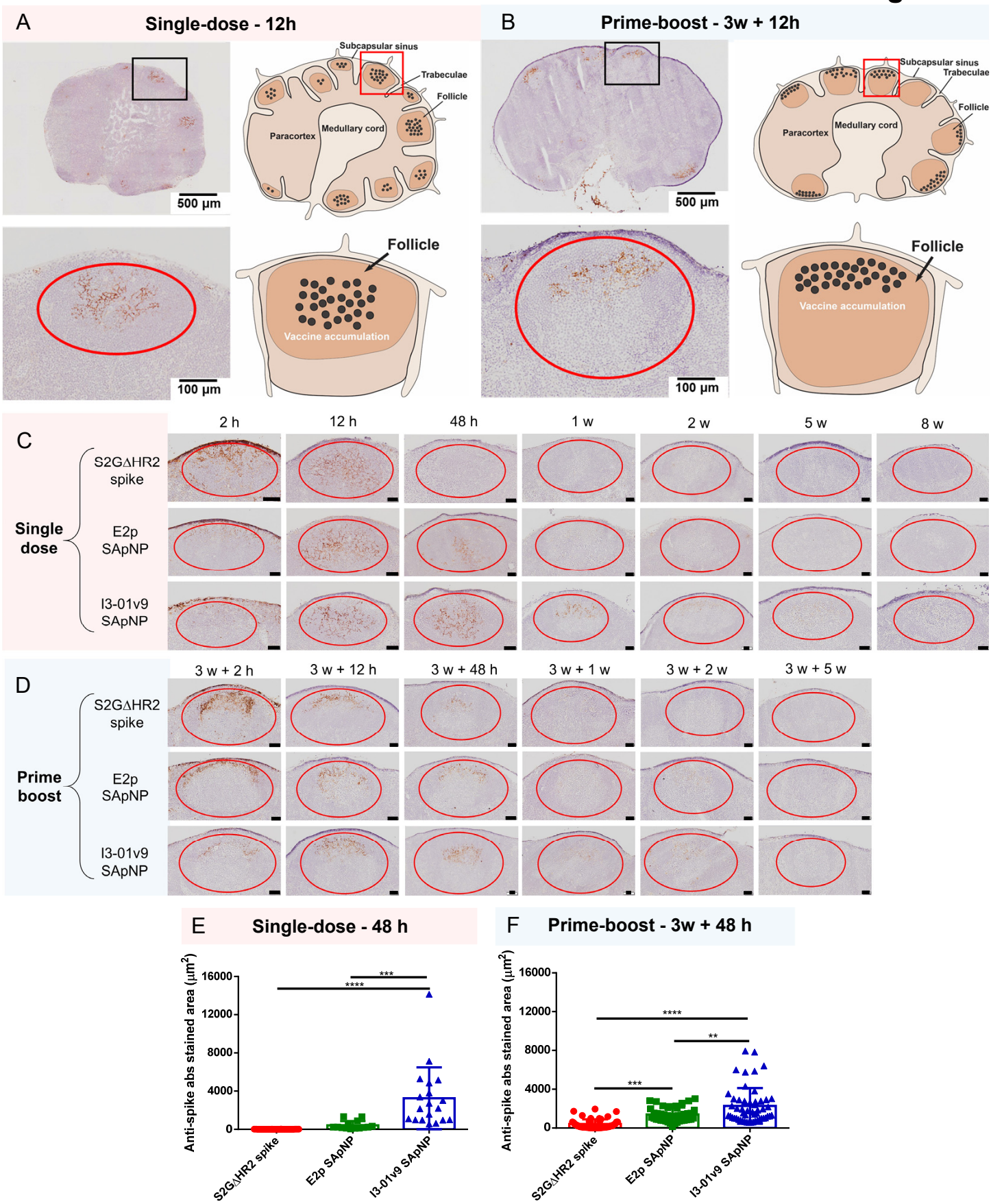

Figure 5

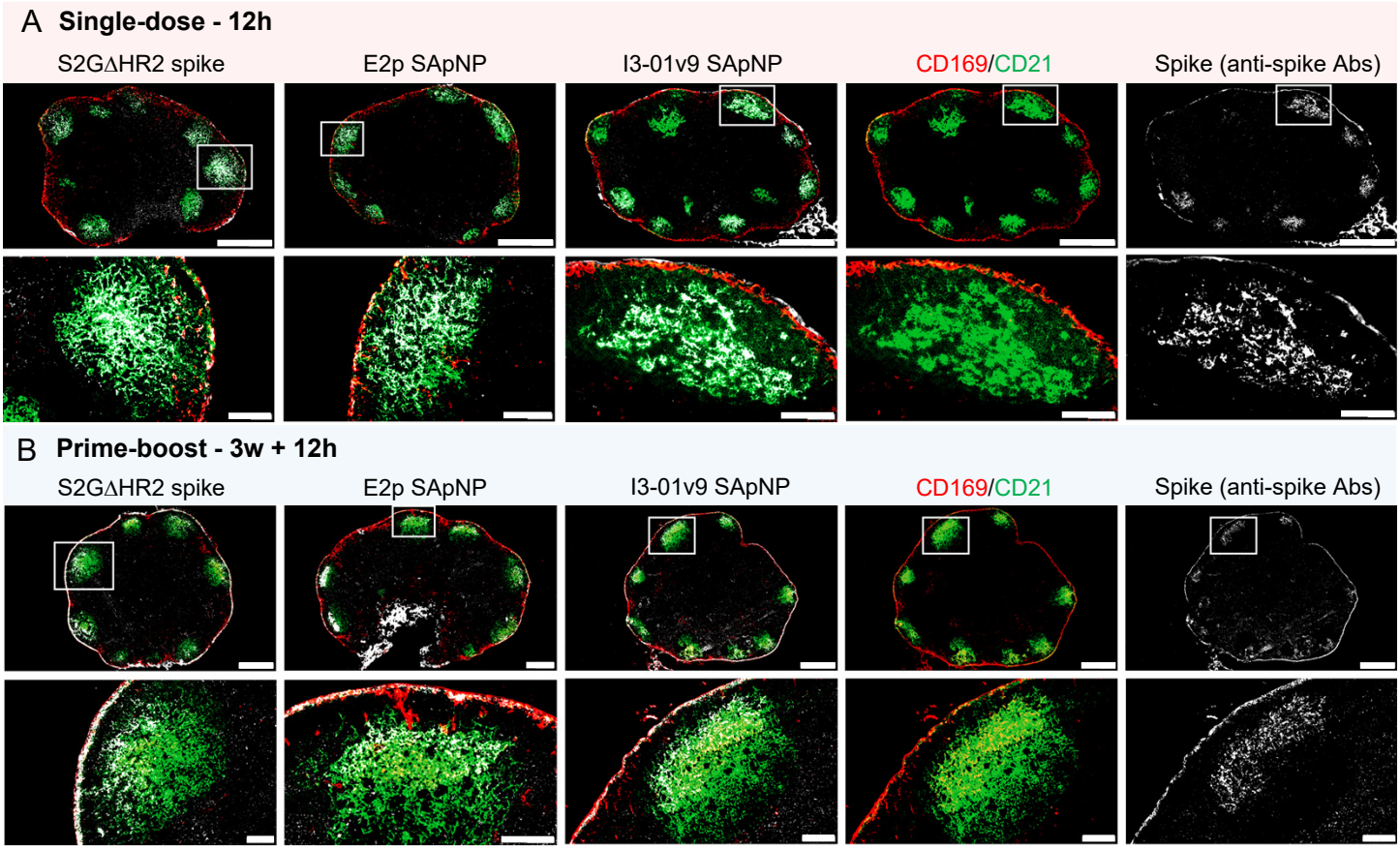

C **I3-01v9 SApNPs (yellow arrow) are aligned on FDC dendrites**

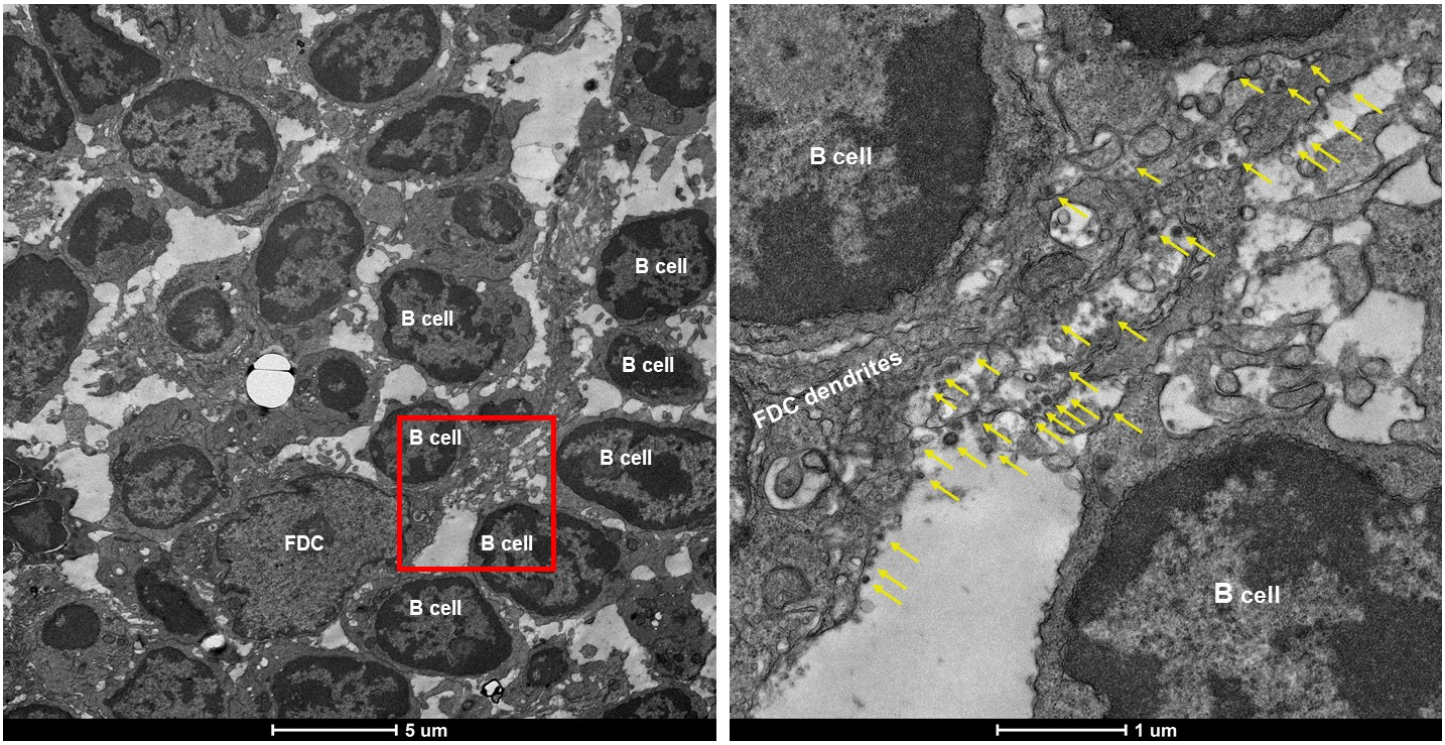

Figure 6